

# Effect of geometry and temper on aluminium plates with pre-cut slits subjected to blast loading

Henrik Granum<sup>a,\*</sup>, Vegard Aune<sup>a,b</sup>, Tore Børvik<sup>a,b</sup>, Odd Sture Hopperstad<sup>a,b</sup>

<sup>a</sup>*Structural Impact Laboratory (SIMLab), Department of Structural Engineering, NTNU, Norwegian University of Science and Technology, Trondheim, Norway*

<sup>b</sup>*Centre for Advanced Structural Analysis (CASA), NTNU, Trondheim, Norway*

## Abstract

In this study, the structural response of 1.5 mm thick aluminium plates with pre-cut slits subjected to blast loading is studied. The plates were tested in three different tempers with four different pre-cut slit geometries at two different firing pressures in a shock tube facility. High-speed cameras and pressure sensors recorded the blast event and together with 3D digital image correlation and 3D scan were used to study the response of the plate. Both the pre-cut slit geometries and the tempers were seen to influence the structural response of the plates. The tests suggest that the material strength is of less importance, while ductility is seemingly important for the plates' resistance to crack propagation. The velocity of the propagating cracks were higher for plates with high strength and low ductility when compared to a test where the plate had contrary material properties. Quasi-static tensile tests were conducted to calibrate the constitutive model and the failure criterion by use of inverse modelling in the optimization tool LS-OPT. A finite element model of the blast exposed area was made in Abaqus/Explicit and a sensitivity study conducted to investigate the influence of the element size and meshing technique on the response. The results from the numerical simulations were overall in good agreement with the experimental results, and it was evident that the simple model gave accurate results in most of the cases, however, discrepancies were found.

## 1 Introduction

Plates subjected to blast loading has been an important subject of research over the years to develop protective structures and ensure peoples safety. Among the different blast events, the one where the blast load is combined with fragments is the most detrimental. These fragments may perforate the structure, reducing the capacity significantly which is important to include in the design of blast-resistant structures. A possibility to make the problem more feasible is to inflict damage to the structure prior to testing, in an attempt to mimic the effect of fragments. Rakvåg et al. [1] tested steel plates with

---

\*Corresponding author.

E-mail address: [henrik.granum@ntnu.no](mailto:henrik.granum@ntnu.no) (Henrik Granum)

URL: <http://www.ntnu.edu/kt/fractal>

four different pre-cut geometries subjected to blast loading, i.e., square, circle, diamond and slit. The firing pressures tested were not sufficient to initiate fracture in the plates, but revealed a difference in the deflection for the different pre-cut geometries. Lagrangian and coupled Eulerian-Lagrangian simulations were conducted to study the effect of fluid-structure interaction (FSI). The Lagrangian simulations were overall in good agreement with the tests, but the deformation in the vicinity of the pre-cut holes was not accurately predicted. By including the FSI effect in the coupled simulations, the deformation increased compared to the Lagrangian simulations as expected, and revealed that the pressure around the pre-cut holes was higher than for the rest of the plate. The simulations showed that the configuration with pre-cut slits resulted in high levels of localized equivalent plastic strain as opposed to the circular holes, where the levels were reduced with a factor two when compared to each other. This suggested that the plate with pre-cut slits was more susceptible to fracture than the other pre-cut geometries tested. Li et al. [2] tested three different pre-cut geometries subjected to three different TNT mass detonations. For two of the configurations (square and circular holes) no failure was observed in any of the tests, while for the diamond-shaped configuration, failure was observed in all tests. This substantiates the presumption by Rakvåg that the shape of the pre-cut holes is important for failure. Aune et al. [3] studied steel plates with and without pre-cut square holes subjected to blast loading. The plates were tested at four different pressures, resulting in no fracture for the lowest pressure and complete failure for the highest pressure for the plates with pre-cut holes. In the tests at the two intermediate pressures, cracks initiated at the corners of the holes and propagated towards the centre and corners of the plate. For the full plates, no failure was found in any of the tests at all the tested pressures. Lagrangian simulations with a refined mesh were able to predict the damage evolution, however, the plate response was overestimated in some cases. Zhang et al. [4] investigated I-core sandwich panels subjected to combined blast and fragment loading. Pre-fabricated fragments and high-explosives were used to generate the load, and the results were compared to tests where only high-explosives were used. It was reported that the damage caused by the combined blast and fragment loading was more severe and led to perforations of the panels, reducing the capacity sufficiently to enable tearing of the panels as the failure mode.

The literature on plates subjected to blast loading mostly focuses on the loading and/or the structural response of the plate. The effects related to the material properties of the target material are rarely investigated in these studies. Langdon et al. [5] studied plates of five different materials subjected to blast loading. The strength and ductility of the materials differed considerably and the plates were tested with varying thicknesses and planar dimensions. The tests were conducted using high explosives where the charge mass, diameter of charge and stand-off distance were varied to obtain different load conditions. Ductility was pointed out as an important property to prevent rupture of the plates and the results suggested that there was a correlation between energy absorbing capabilities and blast performance. However, they were not successful in correlating the material properties with the rupture performance.

For ballistic impact, the influence of material properties have been studied in numerous cases. Holmen et al. [6] showed that material strength is the governing material parameter regarding perforation resistance when struck by small-arms bullets. This was explained by the highly localized process taking place when a small-arms bullet perforates a target plate. However, studies with larger projectiles at lower velocities suggest that there is a combined dependency from both strength and ductility (see e.g. [7] and [8]), and under certain conditions such materials may perform better than materials with high strength and low ductility.

Granum et al. [9] studied quasi-static axial crushing of aluminium profiles of three different alloys in three different tempers, where strength, ductility and work hardening varied among the alloys and tempers. The energy absorbing capabilities were found to mainly depend on the strength of the material, however, ductility is important to avoid peeling and fragmentation of the profile which may reduce the energy absorbing capabilities.

The experimental objective in this study is to investigate how the number and orientation of the slits and temper of the plate affect the structural response. Uniaxial tensile tests are conducted in three directions with respect to the rolling direction to calibrate a constitutive model and a failure criterion used in the numerical analysis. In the numerical part of the study, the predictive capabilities of the numerical simulations are evaluated and discussed when compared to the blast tests.

## 2 Material

### 2.1 Material and material tests

The plates were received with dimensions 625 mm × 625 mm × 1.5 mm cut from the rolled and heat treatable aluminium alloy AA6016 produced by Hydro Aluminium. This alloy is popular for use in the automotive industry due to its good formability, decent strength and high corrosion resistance. The alloy is particularly suited for inner and outer body components where long and high temperature paint bake cycles may occur. The plates were received in three different temper conditions, i.e., the solution treated T4 temper and the artificially aged T6 and T7 tempers. The T4 temper alloy was solution treated at 530°C, air quenched and naturally aged. The peak strength T6 temper was obtained by heating at 185°C for five hours and the over-aged T7 temper at 205°C for 24 hours after solution treatment and quenching. The chemical composition of the alloy is given in Table 1.

Table 1: The chemical composition of AA6016 in wt-%.

| Si     | Mg     | Fe     | Cu     | Mn     | Cr     | Zn     | Ti     | Al      |
|--------|--------|--------|--------|--------|--------|--------|--------|---------|
| 1.3160 | 0.3490 | 0.1617 | 0.0081 | 0.0702 | 0.0025 | 0.0084 | 0.0175 | Balance |

A plate in each temper was used to manufacture specimens for tensile tests. Dog-bone specimen with a gauge length of 70 mm and an initial thickness 1.5 mm were cut out with orientation  $0^\circ$ ,  $45^\circ$  and  $90^\circ$  with respect to the rolling direction. A sketch of the geometry of the specimen can be found in [10]. The thickness of the specimen was measured at three different places in the gauge section of each specimen. Three tests for each temper and orientation were conducted, resulting in a total of 27 tensile tests. The tensile tests were conducted in an Instron 5982 universal testing machine with a 100 kN load cell at an initial strain rate of  $5 \times 10^{-4} \text{ s}^{-1}$ . The force was recorded by the load cell and a camera oriented perpendicular to the specimen captured pictures, both synchronized at 1 Hz. All specimens were spray-painted with a speckle pattern to enable 2D-DIC to track displacements by use of the in-house DIC code, eCorr. The DIC code as well as the method used in this study is presented in detail in [11]. The displacement was tracked by use of a virtual extensometer with an approximate length of 50 mm. The force-displacement curves for representative tests in all directions are shown in Figure 1a all the way to failure. The calibration of the hardening parameters was performed on the representative test in the rolling direction for each temper and a plot of the engineering stress-strain curves from the experiments and the simulations is shown in Figure 1b. The circle denotes the assumed point of fracture based on the experimental results. The calibration of the constitutive model is explained in detail in Section 5.2.

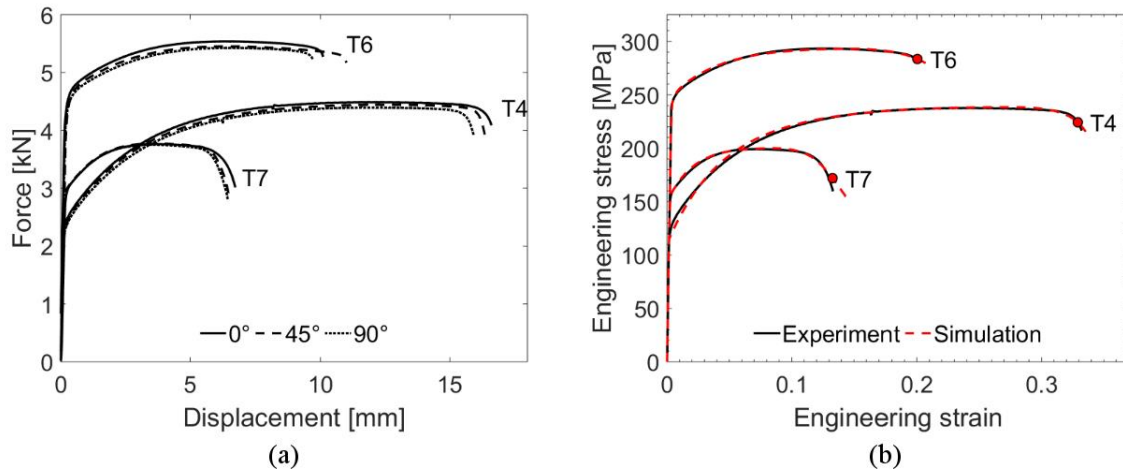


Figure 1: (a) Force-displacement curves of representative tests in each direction and (b) engineering stress-strain curves of experiment and simulation.

Negligible anisotropy is seen with respect to the flow stress, while the elongation at failure is seen to vary, both within and between directions. The flow stress ratio  $r_\alpha = \frac{\sigma_\alpha}{\sigma_0}$  was calculated, where  $\alpha$  is the angle with respect to the rolling direction and  $\sigma_0$  is the yield stress in the rolling direction. The flow stress ratios for the different directions and tempers were found to be practically constant, deviating from 0.97 for  $r_{90}$  in T7 temper to unity. A virtual extensometer was employed to measure the strain in

the width direction during a test and the plastic strain ratio  $R_\alpha = \frac{d\varepsilon_w}{d\varepsilon_t}$  was calculated by assuming plastic incompressibility and is shown in Table 2. The plastic strain ratios  $R_\alpha$  display minor variations in the evolution of the strain in the different directions. The R-values are consistently highest in the rolling direction, and shows that there is a slight anisotropic behaviour of the material.

Table 2: Plastic strain ratio  $R_\alpha$  from representative tensile tests.

|    | 0°   | 45°  | 90°  |
|----|------|------|------|
| T4 | 0.58 | 0.45 | 0.44 |
| T6 | 0.69 | 0.48 | 0.55 |
| T7 | 0.77 | 0.57 | 0.62 |

The diffuse necking in the rolling direction of the tensile tests occurred at a plastic strain of 0.216, 0.119 and 0.066 for the T4, T6 and T7 temper, respectively. The Considère criterion  $d\sigma/d\varepsilon_p = \sigma$  predicts diffuse necking at a plastic strain of 0.239, 0.135 and 0.079 based on the calibrated Voce curves for the T4, T6 and T7 temper, respectively. The Considère criterion consistently predicts diffuse necking at a slightly larger plastic strain than what found in the tensile tests.

### 3 Shock tube setup and programme

#### 3.1 SIMLab Shock Tube Facility

The experimental programme of the blast loaded plates were conducted in the SIMLab Shock Tube Facility (SSTF) at NTNU. A detailed description of the SSTF as well as a validation of the facility can be found in Ref. [12]. A general overview of the SSTF and its components is shown in Figure 2. The tube is made of stainless steel and is divided into three main parts. At the left end, a high-pressure chamber denoted the driver section is located which by use of removable aluminium inserts obtains a length of 0.77 m. The driver section is separated from the rest of the tube by the firing section which consists of several intermediate chambers separated by diaphragms. Following the firing section is a low-pressure chamber denoted the driven section where the test specimen is mounted to the end. The length of the driven section is 16.2 m. The intention with multiple chambers in the firing section is to create a step-wise pressure gradient between the driver and driven sections where initiation of the shock wave is controlled by venting of this section, resulting in a controlled rupture of the diaphragms. The resulting shock wave travels towards the specimen simultaneously as rarefaction waves travels in the opposite direction. These rarefaction waves are reflected at the rear end of the driver section and chases the shock wave towards the specimen. By keeping the length of the driver section short compared to the driven section, the rarefaction waves catch up with the shock wave, resulting in pressure-time history similar to that in a free-field airblast explosion. The test specimen is attached to the flange of the tube by use of two clamping frames and twelve M24 bolts as depicted in Figure 3a, in an attempt to achieve

fixed boundary conditions. All plates tested in this study were mounted with the rolling direction along the vertical direction. The planar shock wave impacts the plate where the exposed area corresponds to the internal cross-section of the driven section, viz.  $0.3\text{ m} \times 0.3\text{ m}$ . Upstream the driven section, two pressure sensors denoted Sensor 1 and Sensor 2 are located  $0.245\text{ m}$  and  $0.345\text{ m}$  from the test specimen, respectively, to obtain pressure-time histories close to the test specimen during testing. The test specimen is covered by a dump tank with windows on each side, allowing high-speed cameras to record the test. Two Phantom v1610 high-speed cameras was positioned according to Figure 2 in a symmetric stereovision setup, recording the blast event at  $24\,000\text{ fps}$  with an image size of  $768 \times 800$  pixels. The testing was conducted in two parts, and prior to the second part, the two high-speed cameras were upgraded to Phantom v2511 and in the following tests the event were recorded at  $37\,000\text{ fps}$ . The images were synchronized with the pressure measurements from Sensor 1 and Sensor 2 for all tests. Three-dimensional digital image correlation (3D-DIC) analyses were conducted using the high-speed camera images. The same in-house DIC code as used in the 2D-DIC was employed here. The stereovision setup was calibrated prior to testing by a pre-calibrated cylinder with a diameter of  $80\text{ mm}$  and a checkerboard pattern printed on the surface. In total, five pictures with varying position of the cylinder was used in each of the calibration processes. Out-of-plane displacements were calculated based on the image sets from the two synchronized cameras, comparing the relative displacement of the plate at the deformed state to an undeformed reference state. Prior to each test, the plates were spray-painted with a speckle pattern. The axial movement of the entire tube was measured and accounted for in the results from the analyses.

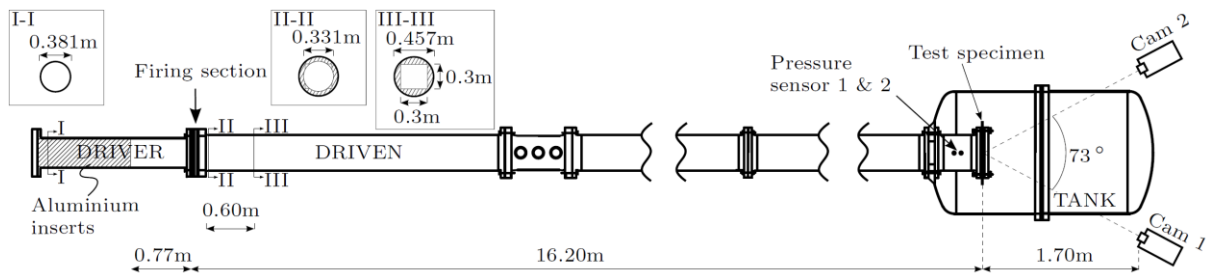


Figure 2: Overview of the SIMLab Shock Tube Facility (SSTF) [3].

### 3.2 Blast test programme

The blast test programme was conducted in two parts, where part one tested plates in T4 temper at two different firing pressures,  $1.0\text{ MPa}$  and  $1.5\text{ MPa}$ . The objective with part one was to investigate the influence of the slit geometry on the structural response of the plate and based on that, choose geometries for further testing on plates in other tempers. In particular, propagation of cracks and the fracture mode were of interest. The four different geometries tested are shown in Figure 3b. Part two of the study focused on the influence of temper on the structural response of the plates. The two chosen geometries were tested in two additional tempers, i.e., T6 and T7. Allowing us to investigate

if the material properties influence the structural response of the plate, and compare them to the results from part one of the study. An overview of the blast test programme is shown in Table 3 and consists of eight tests in part one and eight tests in part two for a total of 16 tests. Each test is given an abbreviation which is used for the rest of this study.

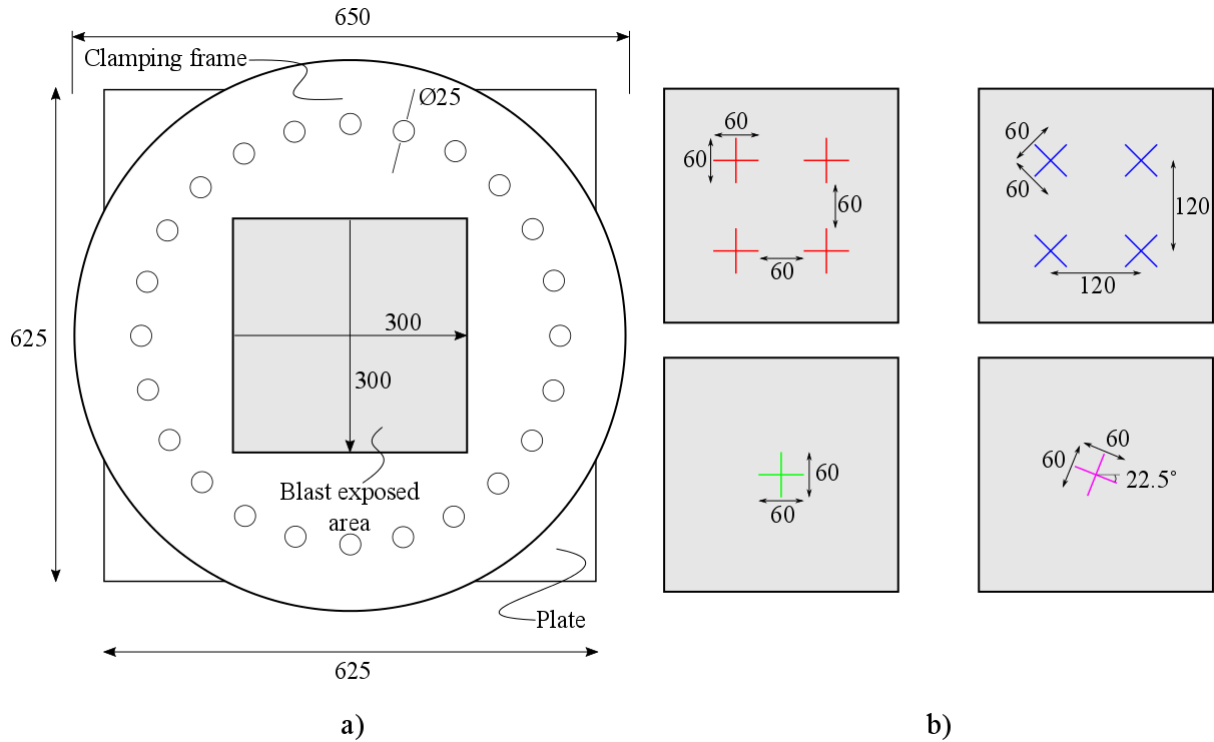
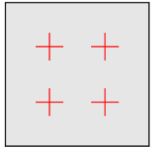
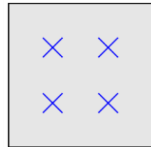
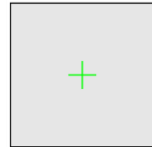
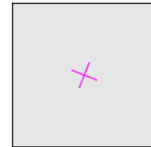


Figure 3: Sketch of a) plate and clamping frame and b) blast exposed area of the plates depicting the four pre-cut slit(s) geometries. Measures are in mm.

Table 3: Overview of the blast test programme.

| Firing pressure<br>[MPa] |  |  |  |  |
|--------------------------|---|---|--|---|
| 1.0                      | T4-4-HV-1.0   | T4-4-45-1.0   | T4-HV-1.0  | T4-22.5-1.0   |
|                          |   | T6-4-45-1.0   |  | T6-22.5-1.0   |
|                          |   | T7-4-45-1.0   |  | T7-22.5-1.0   |
| 1.5                      | T4-4-HV-1.5   | T4-4-45-1.5   | T4-HV-1.5  | T4-22.5-1.5   |
|                          |   | T6-4-45-1.5   |  | T6-22.5-1.5   |
|                          |   | T7-4-45-1.5   |  | T7-22.5-1.5   |

## 4 Experimental results

### 4.1 *Effect of geometry*

Figure 4 shows the deformed state of the T4 plates with one slit at the two firing pressures. By inspection of the figure it is evident that the plate with the slit rotated  $22.5^\circ$  experienced more failure than the plate where the slit were oriented along the horizontal and vertical axis. The difference is less pronounced at the lowest firing pressure, where both slit configurations experienced minor propagation of cracks along the slit directions. However, for the highest firing pressure there is an evident difference, where the integrity of the plate is lost in the T4-22.5-1.5 test. The cracks paths are curved and seemingly seeking towards the corners of the plate, resulting in complete failure for this plate. In the T4-HV-1.5 test, the cracks are seen to propagate along the slit directions, as for the lower firing pressure. However, compared to the T4-22.5-1.5 test, the damage on the plate is prominently less and the plate have not experienced complete failure. In all tests, the plates are seen to deform in a petal deformation where flaps in the vicinity of the slits are folded and the pressure is partially ventilated through the resulting opening.



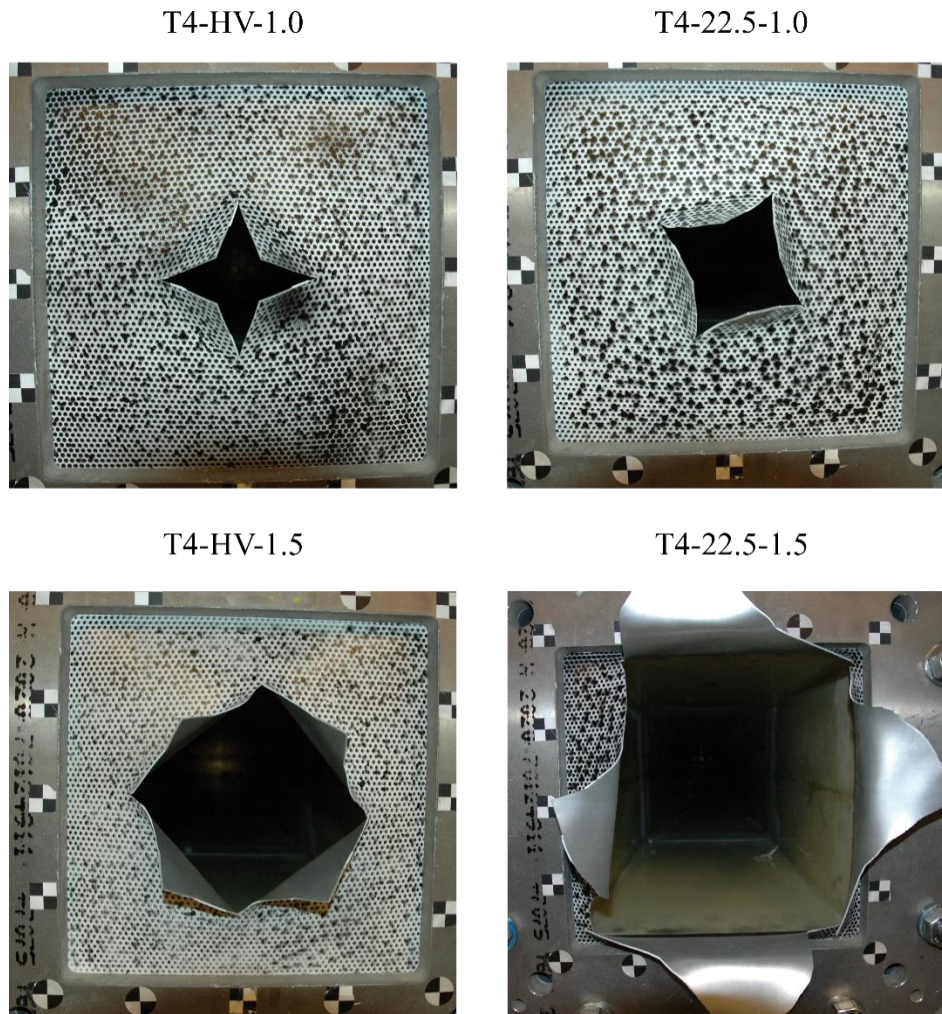


Figure 4: Deformed state of plates with one slit.

In Figure 5 the deformed state of the plates with four slits are shown 1.5 ms after impact. Three of the four tests are about to experience complete failure, while one is only experiencing minor crack propagation. The effect of the orientation of the slits is negligible at the highest firing pressure, while there is a considerable difference at the lowest firing pressure. The failure pattern for the T4-4-HV tests are similar, where the cracks propagated in the slit directions. The only differences between these two tests based on the observations in Figure 5 are the slightly longer propagated cracks in the T4-4-HV-1.5 test as well as the out of plane displacement of the centre square of the plate. In both tests the failure pattern is the same, where the centre square of the plate is torn out and the remainder of the plate is folded around the clamping frame. In contrast to the T4-4-HV tests, the T4-4-45 tests exhibit differences between the two firing pressures. For the lowest firing pressure, only minor crack propagation and a petal deformation around the slits are seen, whereas for the highest firing pressure cracks between the slits fuse, resulting in the centre part of the plate being torn out in the shape of a cross. Cracks propagate from the slits oriented towards the corners of the plate all the way to the corner and the remainder of the plate is folded around the clamping frame. In the T4-4-45-1.0 test, both curved and straight crack

paths are seen, and no symmetry or system of the crack paths was found. However, the T4-4-45-1.5 test exhibit a double-symmetric failure mode.

Based on these results it is difficult to conclude if increasing the amount of slits or changing the orientation of the slits is more detrimental, as both proved to have an impact on the response. When the slits are oriented along the horizontal and vertical axis, the results suggests that increasing the amount of slits is more detrimental as expected, analogous to increasing the amount of damage in the plate. However, the impact of changing the orientation of the slit is also seen to play an important role, independent of the amount of slits.

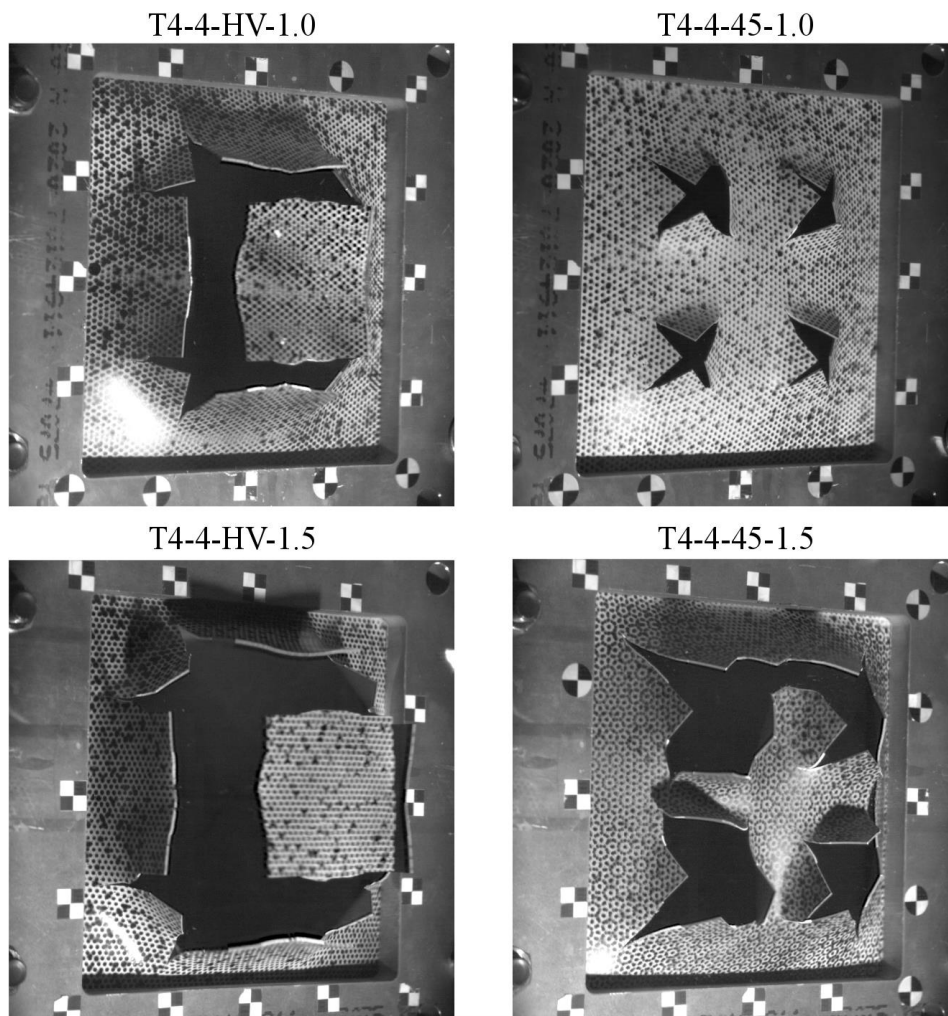


Figure 5: Deformed state of plates with four slits at 1.5 ms after impact.

The pressure-time histories measured by the sensor closest to the plate (Sensor 1) are plotted along with the corresponding massive plate test in Figure 6 and Figure 7 for 1.0 MPa and 1.5 MPa firing pressure, respectively. Sensor 1 is positioned 245 mm upstream the tube, allowing us to study both the incident and reflected shock wave. All data was filtered with a lowpass Butterworth filter of 2<sup>nd</sup>-order

with a cut-off frequency of 0.05 to filter out noise in the recordings. As indicated in the sub plots in the figures, the incident wave is nearly identical within similar firing pressures, substantiating the similar initial conditions among the tests. The peak reflected pressures are also similar, however, for the massive plate tests the pressure is higher compared to the tests due to FSI effects. As expected, the reflected pressures varies among the different geometries, which is related to the varying structural response and FSI-effects of the plates. For the 1.0 MPa firing pressure tests, the T4-4-HV-1.0 test stands out as the reflected pressure drops significantly compared to the other tests, which have similar decay of the pressure over time. This is related to the complete failure in the T4-4-HV-1.0 test, where the shock wave is ventilated into the dump tank as failure of the plate occurred. For the remaining three tests, one can see that the pressure-time curves are shifted compared to the massive plate test, indicating that even though an opening in the plate is created by folding of the flaps, most of the pressure is reflected by the plate. In the T4-4-HV-1.0 test the pressure goes below atmospheric pressure at around  $t = 0.10$  ms, due to over expansion of the shock wave, resulting in a suction in the opposite direction. Among the tests at 1.5 MPa firing pressure, the T4-HV-1.5 test stands out as the shape of the curve is comparable to the massive plate test, only shifted. Meaning that the plate appears to behave similarly as a plate without pre-cut damage and most of the pressure is reflected, even though a substantial part of the plate is folded open. This test is the only test where the fracture does not propagate all the way to the boundary, which allegedly is vital for the shock wave to ventilate into the dump tank.

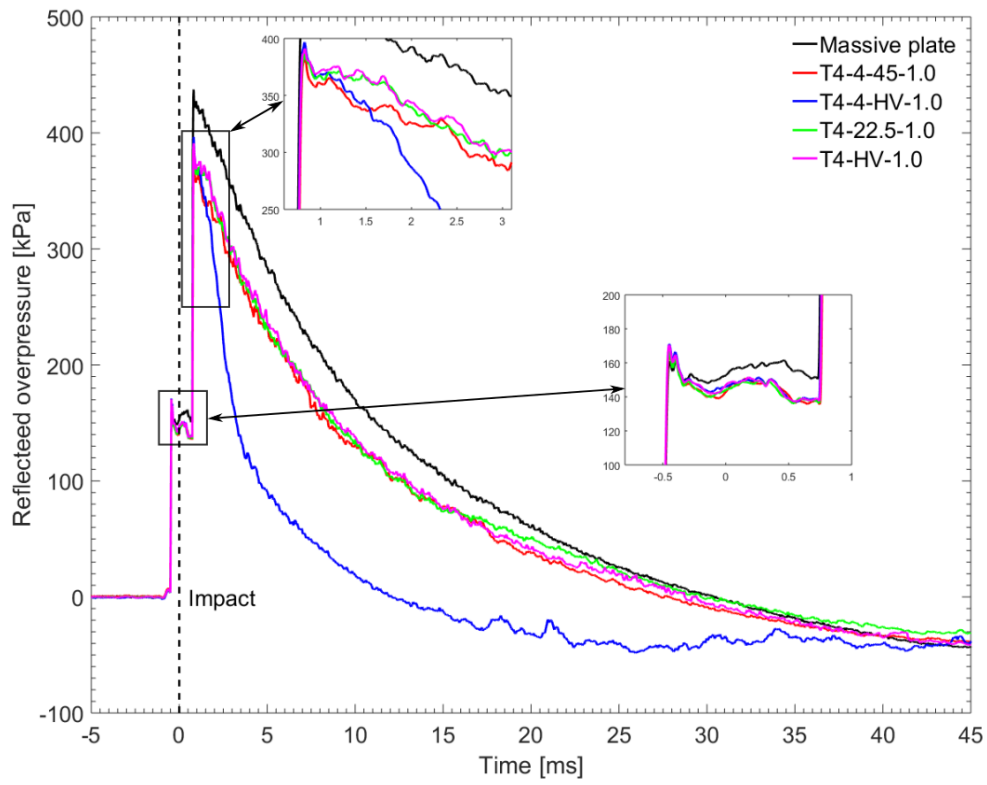


Figure 6: Pressure-time histories from Sensor 1 for the 1.0 MPa T4 tests and corresponding massive plate test. The dashed line indicates the time of impact on the plates.

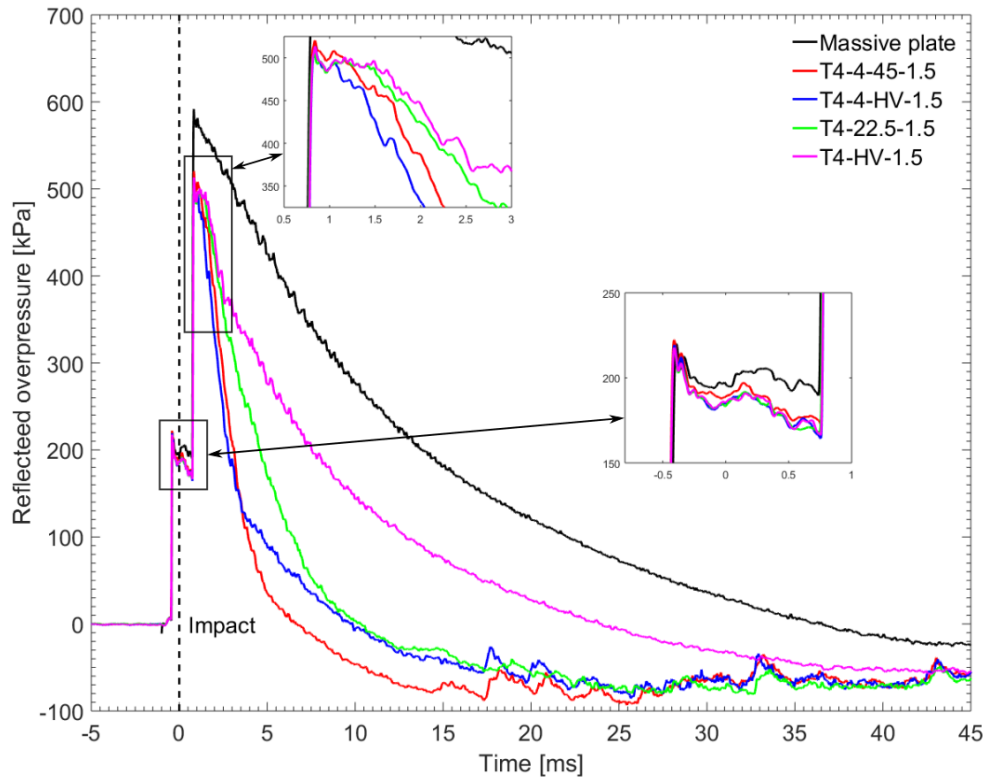


Figure 7: Pressure-time histories from Sensor 1 for the 1.5 MPa T4 tests and corresponding massive plate test. The dashed line indicates the time of impact on the plates.

## 4.2 Effect of temper

Image series from the tests on the different temper plates are shown in Figure 8 to Figure 11 at selected points in time. In general, the T4 and T7 temper plates showed similar behaviour in the four different cases. Both tempers are closer in strength and ductility to each other than to the T6 temper, which have higher strength and lower ductility. The geometry demonstrating the largest differences between the tempers is the 4-45-1.0 tests, where the T6 temper is the only test experiencing complete failure. The deformation is similar up to  $t = 0.75$  ms, but there is already an indication of an incipient crack in the horizontal direction between the two upper slits for the T6 temper, which is not present in the other two tests. The T4 and T7 temper plates exhibit a petal deformation around the slits towards the end of the test, but no prominent crack propagation is seen. After the horizontal crack between the two upper slits fuse, the centre part of the plate is torn out and additional cracks fuse together.

For the 4-45-1.5, 22.5-1.0 and 22.5-1.5 tests, all three tempers gave similar global response, but there are differences in terms of crack propagation and failure between the different tempers. For the 4-45-1.5 tests the failure mode is similar among the three tests and all plates experience complete failure. Based on the images from the high speed camera, cracks are initiating in all three tests at around 0.5 ms

after impact. At  $t = 0.75$  ms, two propagating cracks have already merged for the T6 temper between the two upper slits, while both the T4 and T7 tempers mostly experience petaling deformation around the slits. Even at  $t = 1.00$  ms, no cracks have propagated enough to merge in the T4 and T7 tempers, while in the T6 temper another pair of propagating cracks have merged between the slits on the right side. The same trend is also seen for the cracks propagating along the diagonal towards the corner of the plate, where it is clearly seen that the length of the crack for the T6 temper is longer compared to the T4 and T7 plate at this point in time. At 1.25 ms after impact, all three plates have at least one merged crack and the centre cross is close to being torn out in all cases. The differences between the three plates is less pronounced at this point in time except for the cracks propagating along the diagonals toward the corners of the plate. The T4 and T7 plates give the impression of being more resistant against fracture, even though at  $t = 2.00$  ms the response is nearly identical among the tests.

Some of the trends observed for the 4-45-1.5 tests are also seen in the 22.5-1.0 tests. Based on the high speed images, the cracks initiated at around 0.60 ms after impact for all tests. A mistake was done during testing of the T6-22.5-1.0 tests where the plate was mounted so the slit was oriented in a positive angle as opposed to the other tests with this geometry. This might have altered the results slightly and the results are therefore not emphasized as much with respect to the observed trends. This geometry exhibited the least amount of difference between the different tempers among the tests in this part of the study. The cracks are seen to propagate equally among the tempers at the selected points in time and the final deformation is similar from a global point of view. In the 22.5-1.5 tests, the crack propagation is also initiated at around 0.60 ms after impact for all tests, but already at  $t = 1.00$  ms, the length of the cracks for the T6 temper is considerably longer than what observed for the T4 and T7 tempers. This difference increases somewhat towards the end of the tests, suggesting that the velocity of the propagating cracks are higher for the T6 temper than the T4 and T7 tempers. By close inspection of the high speed images, there is a slight difference in the crack propagation between the T4 and T7 temper, where the velocity of the propagating cracks is slightly lower for the former.

In general, the increased ductility of the T4 and T7 temper compared to the T6 temper is assumed to be decisive to reduce propagation of cracks and increase the capacity of the plate. The higher strength of the T6 temper is not seen to affect the resistance against crack propagation and cracks initiated at the same point in time or earlier compared to the tests with T4 and T7 temper plates. Based on these tests, increased work hardening and ductility is seemingly more important than increased strength with respect to the capacity of the plate. However, we cannot draw definite conclusions based on the limited amount of tests that were carried out and the lack of repetitions.

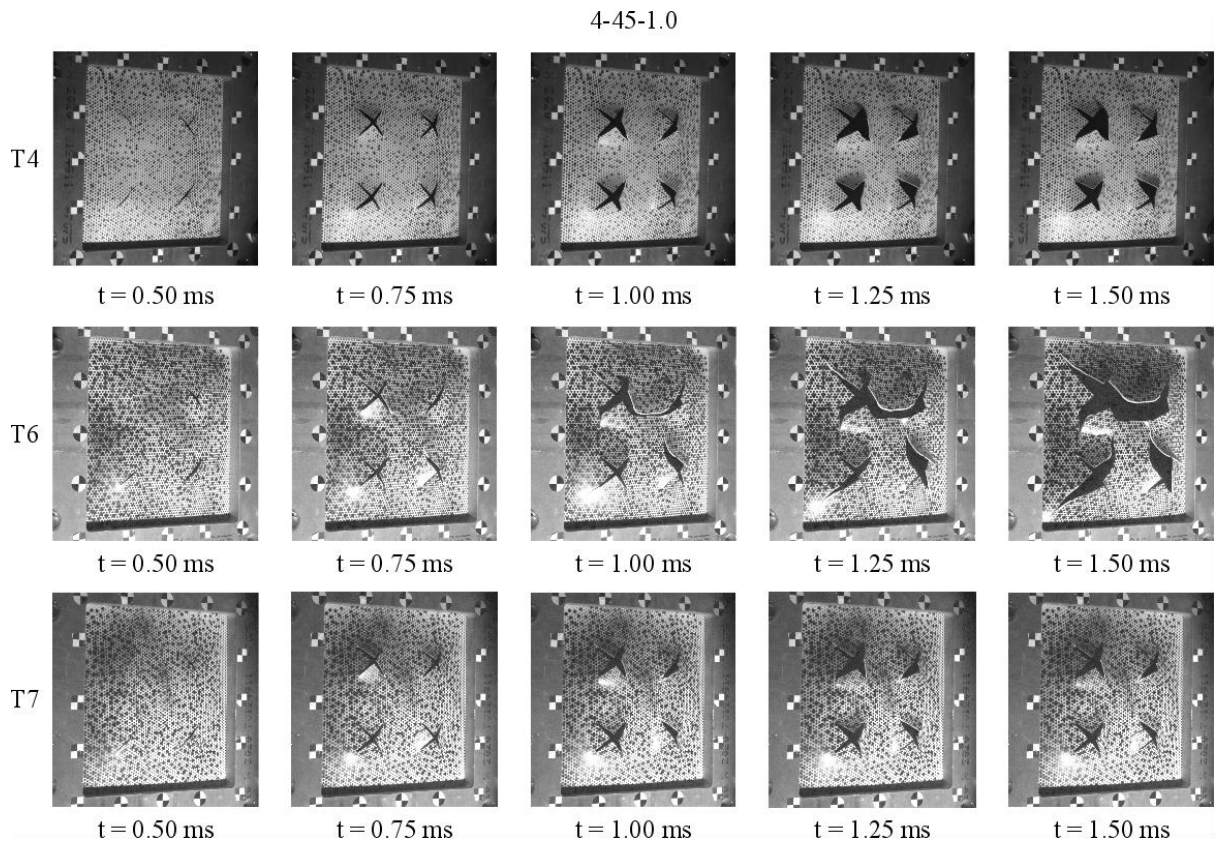


Figure 8: Image series from 4-45-1.0 tests at selected points in time.

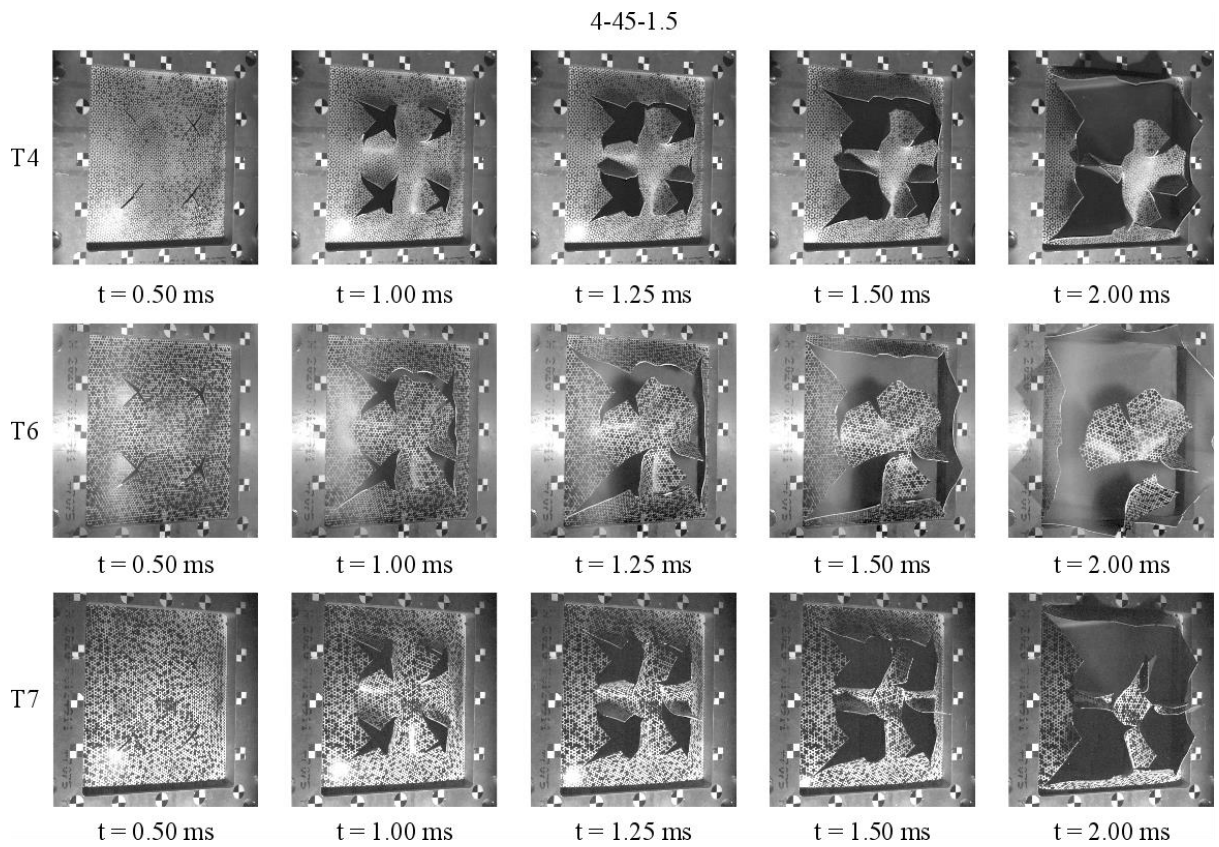


Figure 9: Image series from 4-45-1.5 tests at selected points in time.

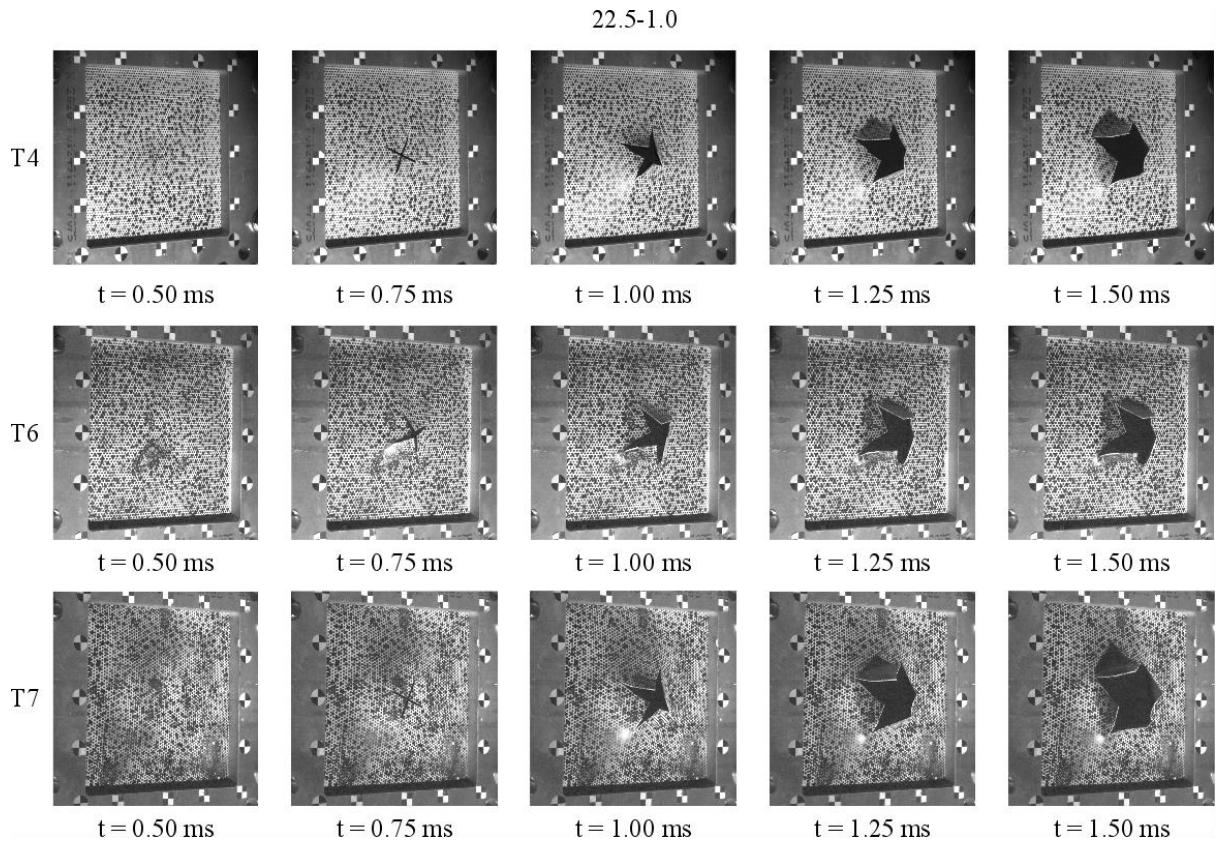


Figure 10: Image series from 22.5-1.0 tests at selected points in time.

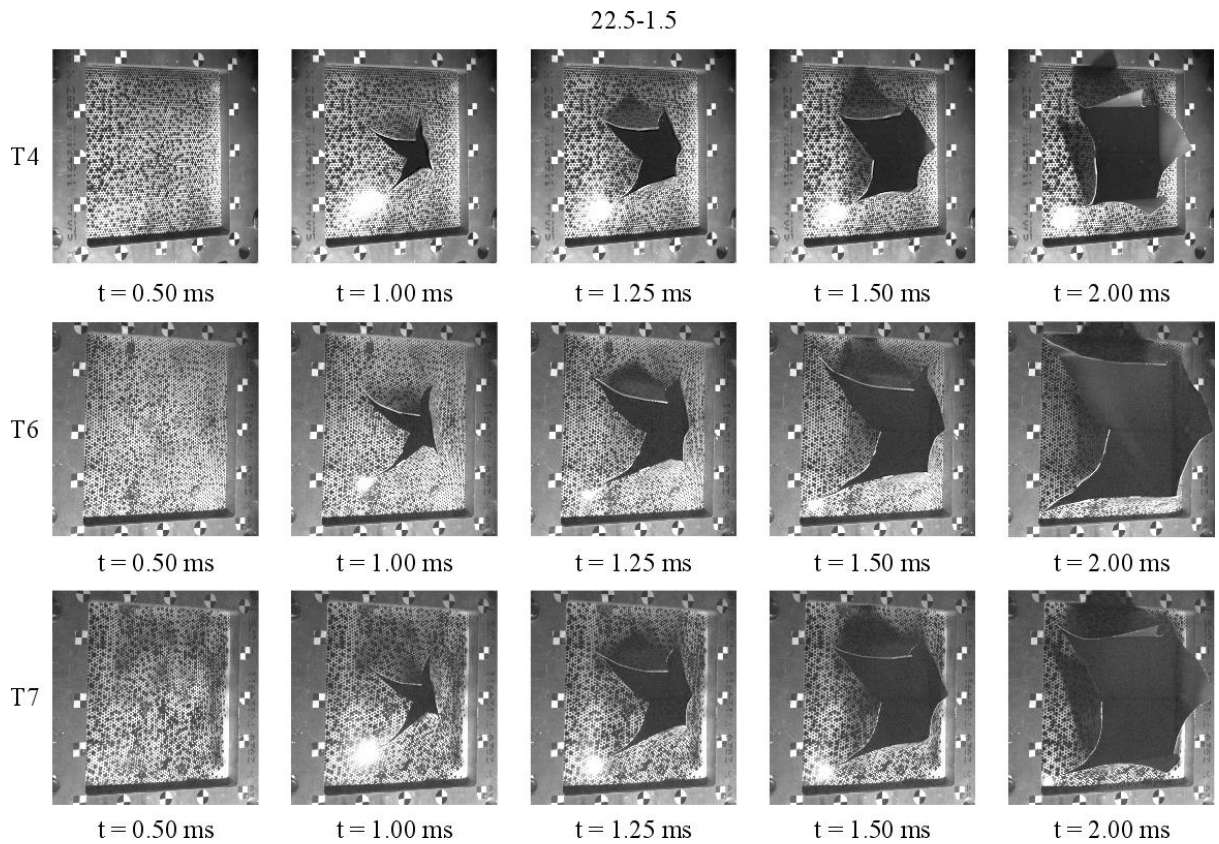


Figure 11: Image series from 22.5-1.5 tests at selected points in time.



### 4.3 3D scan and 3D-DIC

A ROMER Absolute Arm 7252SI was used to scan the plates not experiencing complete failure in the test. The probe was used to define the coordinate axis, while the laser was used to scan the plates. The data was processed by the software PC-DMIS and exported as point clouds and stereolithography files. In Figure 12, the 3D scan of the three 22.5-1.0 tests is compared to each other in terms of front and side images as well as displacement contour plots. By inspection of the images, one can see that the shape of the opening differs among the tests. In the T7 experiment the opening resembles a square, while for the two other tempers the flaps have not folded as much and resembles more of a star shape. In the T6 test the crack paths are more curved than seen for the T4 and T7 tempers, where the crack paths are in the directions of the slits. The length of the cracks were measured, revealing that the T6 temper has the longest crack paths with an average length of 48.5 mm while T7 and T4 tempers have an average length of the cracks with 41.75 mm and 39.5 mm, respectively. When seen from the side, the T4 and T7 temper plates clearly experienced more global response compared to the T6 temper plate, where the deformation is mainly localized in the vicinity of the slits. This is substantiated by the contour plots, where the limits are kept similar for all plots. Keep in mind that that all displacements above 20 mm are not separated from each other, hence the large areas of dark red colour.

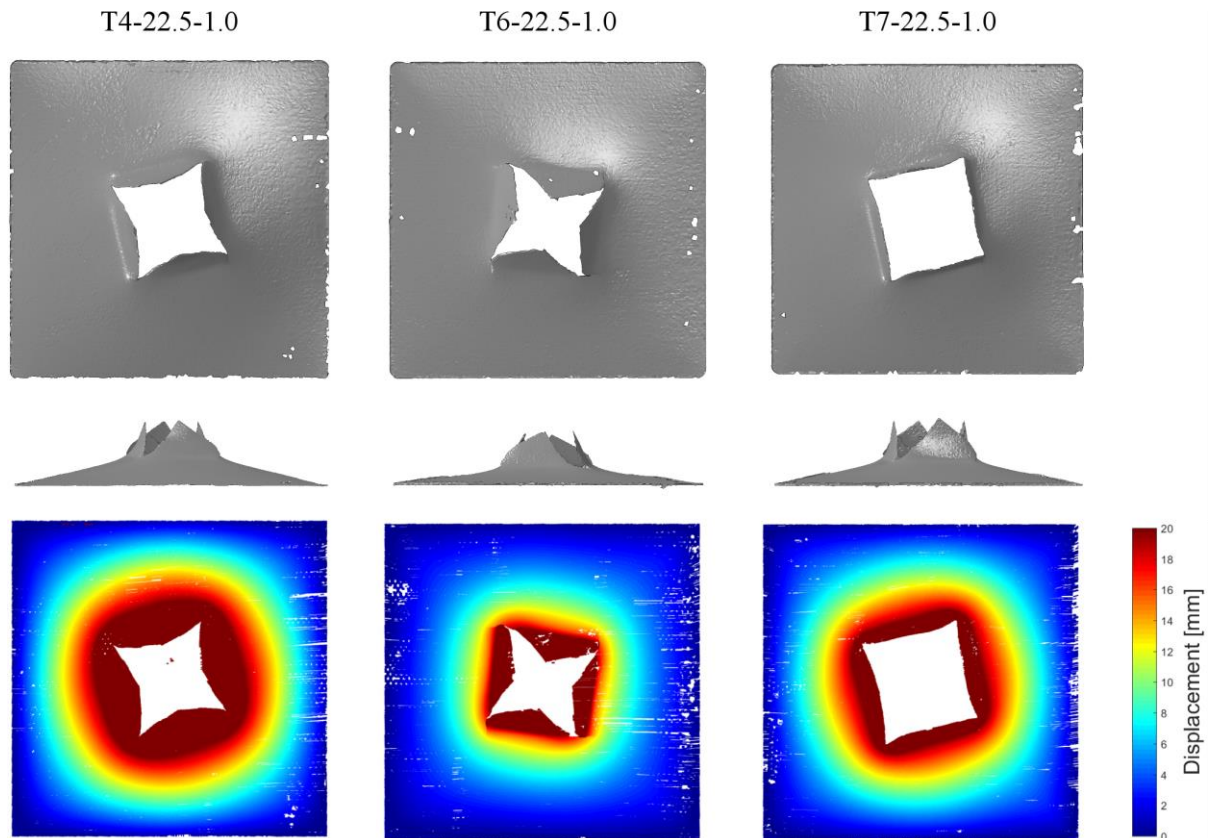


Figure 12: Comparison of 22.5-1.0 tests.

Figure 13 displays the 3D scan of the T4-HV-1.0, T4-22.5-1.0 and T4-HV-1.5 plates. The same global response observed for the T4-22.5-1.0 test is also seen for the T4-HV-1.0 test, visualized by a nearly linear increase in deformation from the boundary towards the centre of the plate. The T4-22.5-1.0 plate folded more around the slits than for the T4-HV-1.0 plate, where the opening in the centre of the plate is more prominent when compared to each other. This is substantiated by the average length of the crack paths, which is 39.5 mm for the T4-22.5-1.0 plate and 26.25 mm for the T4-HV-1.0 plate. The effect of increasing the firing pressure is evident for the T4-HV tests, where both a larger opening of the plate and increased global deformation are seen for the highest firing pressure. The average crack length is 73 mm for the T4-HV-1.5 test, almost three times longer than for the T4-HV-1.0 test.

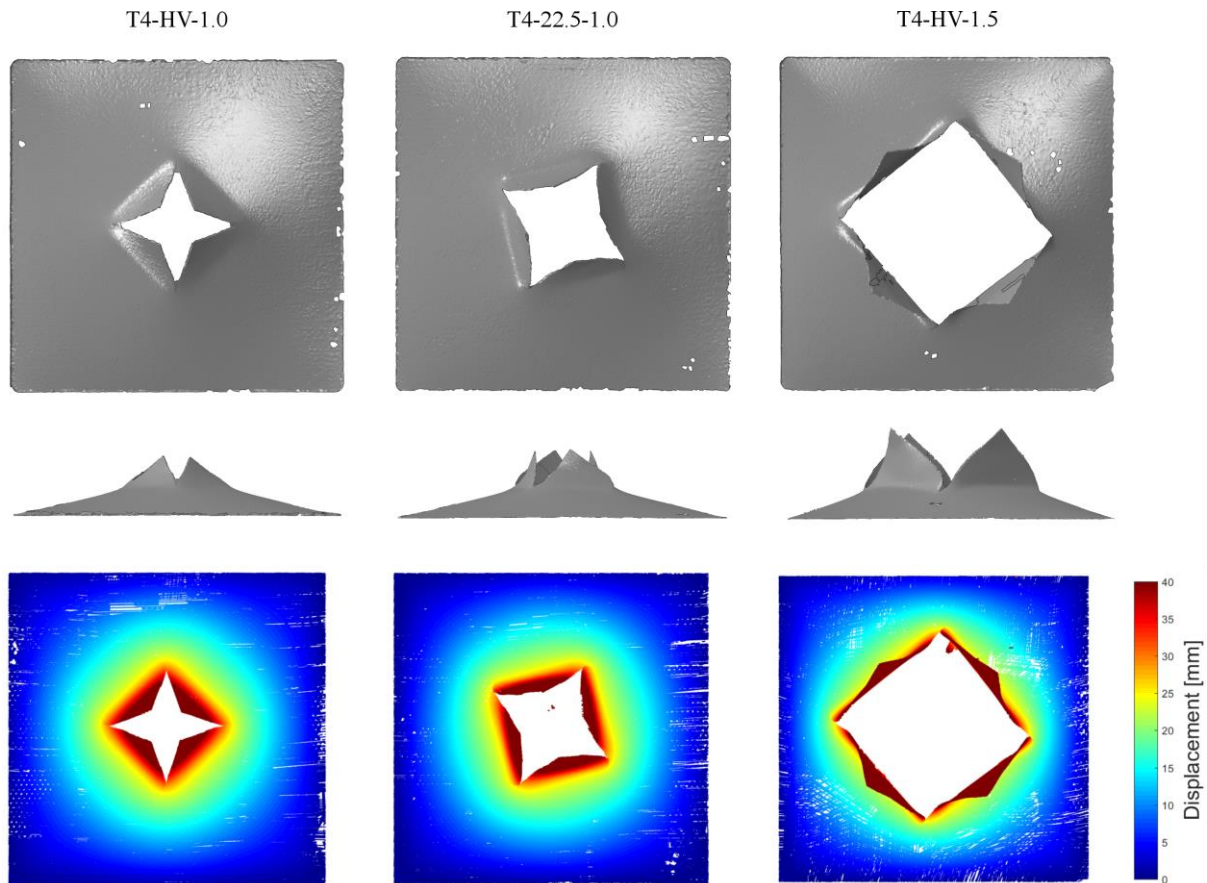


Figure 13: Comparison of tests.

The 3D-DIC technique is used to obtain cross-section displacement profiles during deformation. The cross-section profiles of the centre of the plate are available in two tests, i.e., the T4-4-45-1.0 and T7-4-45-1.0, which are plotted together in Figure 14 at selected points in time. The cross-section is taken from the horizontal axis, denoted x-axis in Figure 14. From the figure one can see the response of the plate is initiated at the boundary and is propagating towards the centre of the plate. The displacement is

consistently larger for the T4 temper compared to the T7 temper, and the difference increases throughout the test. The difference in mid-point deflection at the end is around 5 mm between the two tests.

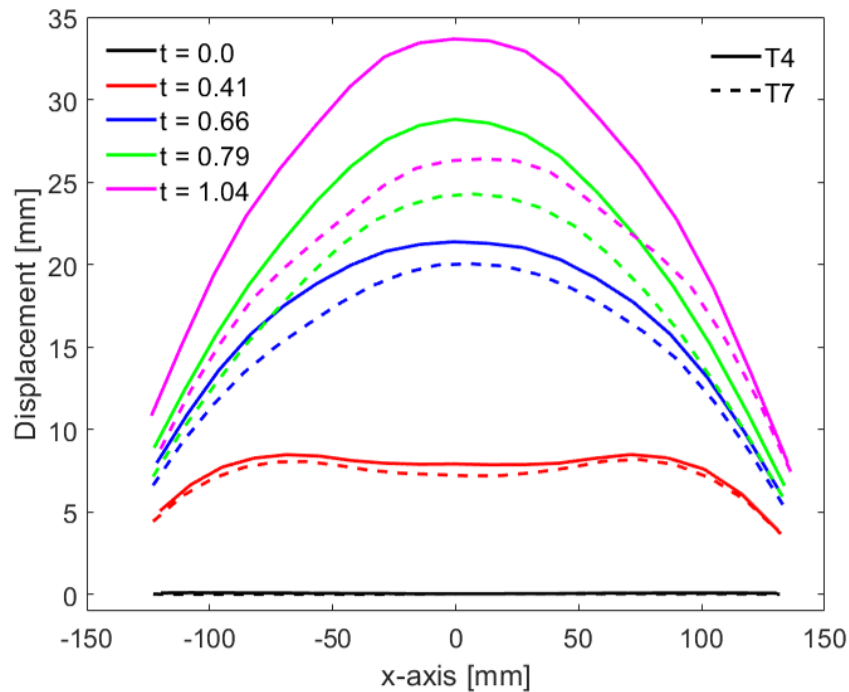


Figure 14: Cross-section profile of 4-45-1.0 test in T4 and T7 temper at selected points in time in ms.

The same observation is made in the 3D scan of the same plates, shown in Figure 15, where the difference in global deformation between the two plates is evident. By inspection of the contour plot one can see that the flaps next to the slits pointing towards the centre of the plate is more deformed than the other. This is also to some extent seen in the side image of the plates. The average crack length is 14.3 mm for the T4 plate and 10.4 mm for the T7 plate. However, the difference in length between the longest and shortest crack within a plate is substantial for these two plates, viz. 16 mm for the T4 plate and 13 mm for the T7 plate. This is related to the varying deformation of the flaps, where the cracks propagating from the slits pointing towards the centre of the plate are consistently longer than the other ones.

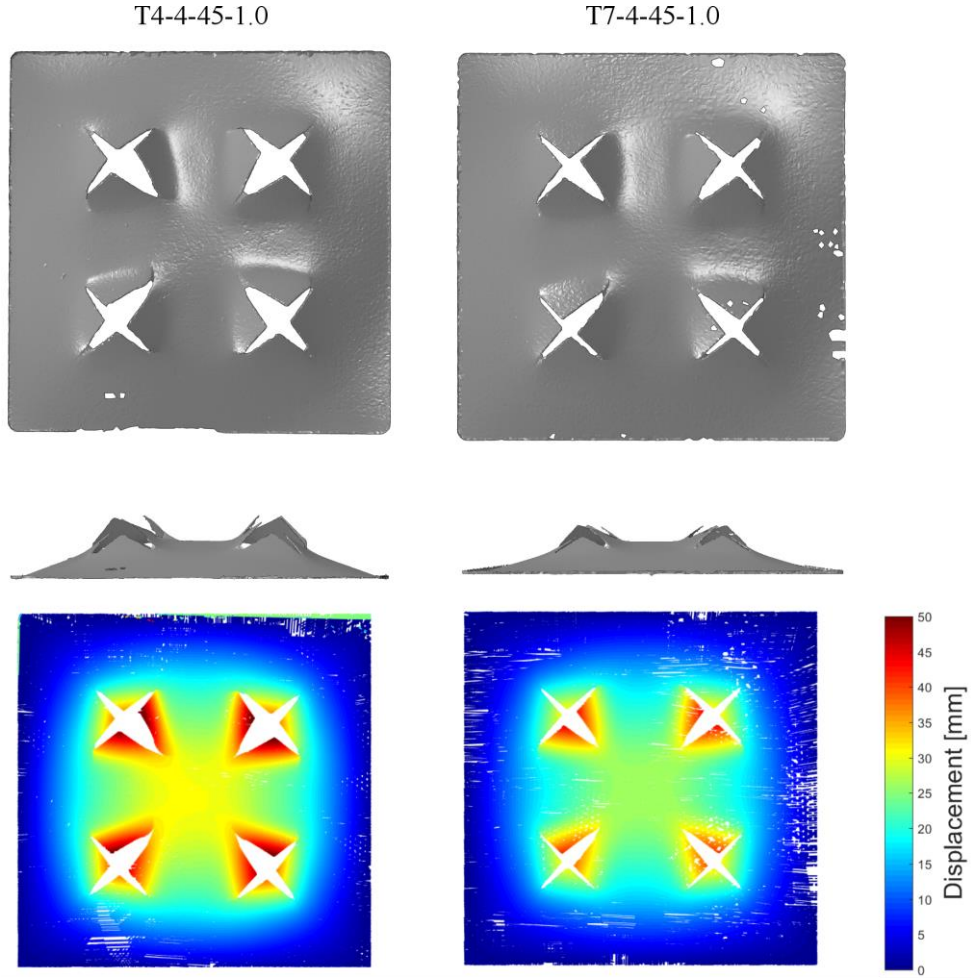


Figure 15: Comparison of 4-45-1.0 tests.

## 5 Material modelling and finite element model

### 5.1 Material modelling

The material behaviour was governed by the modified version of the Johnson-Cook constitutive model where the isotropic work hardening was described by a three term Voce rule [13]. The associated flow rule is assumed and the von Mises equivalent stress is given as

$$\sigma_{\text{eq}} = (\sigma_0 + \sum_{i=1}^3 Q_i (1 - \exp(-C_i p))) (1 + \dot{p}^*)^c (1 - T^{*m}) \quad (1)$$

where  $\sigma_0$  is the yield stress,  $Q_i$  and  $C_i$  are hardening parameters,  $p$  is equivalent plastic strain and  $\dot{p}^* = \dot{p}/\dot{p}_0$  is a dimensionless plastic strain rate, where  $\dot{p}_0$  is a user-defined reference strain rate. The homologous temperature is given as  $T^* = (T - T_r)/(T_m - T_r)$  where  $T$  is the current temperature,  $T_r$  is the ambient temperature and  $T_m$  is the melting temperature of the material. The model parameters  $c$  and  $m$  govern the rate sensitivity and thermal softening of the material, respectively. The change in temperature due to adiabatic heating is calculated as

$$\dot{T} = \frac{\chi}{\rho c_p} \sigma_{\text{eq}} \dot{p} \quad (2)$$

where  $\rho$  is the density,  $c_p$  is the specific heat and  $\chi$  is the Taylor-Quinney coefficient

Failure is taken care of by the uncoupled failure criterion proposed by Cockcroft and Latham (CL) [14], which reads

$$D = \frac{1}{W_c} \int_0^p \langle \sigma_1 \rangle dp = \frac{1}{W_c} \int_0^p \left\langle \sigma^* + \frac{3 - \mu_\sigma}{3\sqrt{3 + \mu_\sigma^2}} \right\rangle \sigma_{\text{eq}} dp \quad (3)$$

where  $D$  is the damage parameter,  $W_c$  is the failure parameter,  $\sigma_1$  is the major principal stress and  $\langle \cdot \rangle$  is the Macaulay brackets which imply that only positive values of the argument contributes. According to the CL criterion, damage evolves for tensile stresses and is driven by plastic dissipation where failure occurs when  $D$  reaches unity in an integration point. The major principal stress can be expressed in terms of the stress triaxiality  $\sigma^*$  and Lode parameter  $\mu_\sigma$  which reads

$$\sigma^* = \frac{\sigma_H}{\sigma_{\text{eq}}}, \quad \mu_\sigma = \frac{2\sigma_2 - \sigma_1 - \sigma_3}{\sigma_1 - \sigma_3} \quad (4)$$

where  $\sigma_1 \geq \sigma_2 \geq \sigma_3$  are the ordered principal stresses and the hydrostatic stress reads  $\sigma_H = (\sigma_1 + \sigma_2 + \sigma_3)/3$ . The dependence on the stress state is governed by the parameters  $\sigma^*$  and  $\mu_\sigma$  and the failure parameter  $W_c$  is a measure of ductility and scales the damage evolution. The fracture surface for the CL criterion as a function of the stress state and the 2D-projections of the fracture locus for chosen values of the Lode parameter is given in Figure 16.

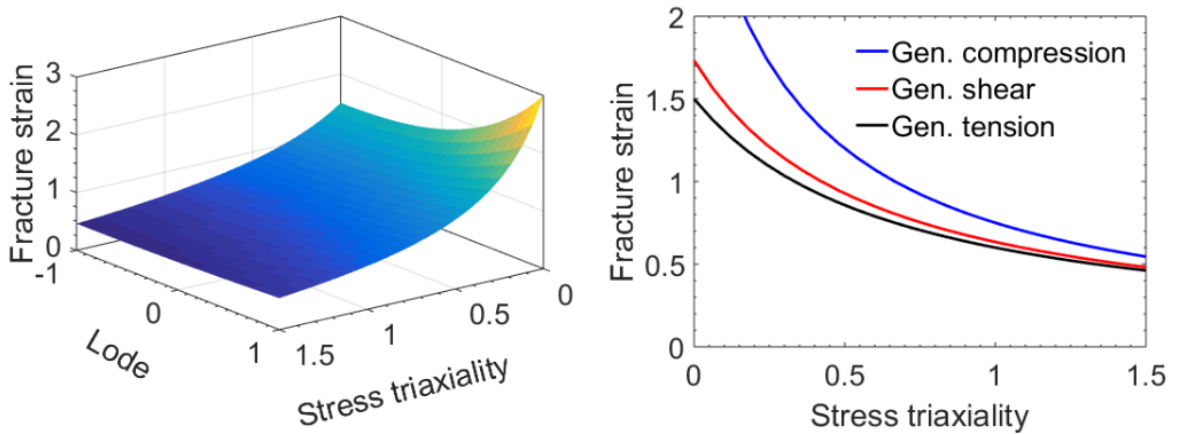


Figure 16: Fracture surface for the Cockcroft-Latham (CL) failure criterion as a function of the stress state and the 2D projections of the fracture locus at selected values of the Lode parameter.

The topology of the fracture surface indicates that the highest fracture strain is observed for generalized compression ( $\mu_\sigma = +1$ ) at low triaxiality, clearly seen in Figure 16b.

## 5.2 Calibration of model parameters

As an initial guess, a least square curve fit of the two first term of the hardening parameters ( $Q_1, C_1, Q_2, C_2$ ) of the extended Voce hardening rule to the true stress-strain curve up to necking was made for the three configurations in a spreadsheet. Only the representative test in the rolling direction was used in the calibration. A FE model of the dog-bone specimen was made in Abaqus/Standard where only a quarter was modeled to save computational time. The mesh consists of 8-node trilinear brick elements with reduced integration where the size of the mesh in the gauge region was 0.1875 mm, giving eight elements over the thickness. Calibration of the hardening parameters was done in the optimization tool LS-OPT, where sequential simulations on the same model were run with different choices of the hardening parameters. The initial guess obtained from the curve fit up to necking was used as starting values, where the first term of the hardening parameters, ( $Q_1, C_1$ ) were fixed, while the two remaining terms ( $Q_2, C_2, Q_3, C_3$ ) were allowed to change. The engineering stress-strain curves up to failure were used as target curves in the optimization. A genetic algorithm was applied in the optimization where 100 equidistant regression points were used in the calculation of the mean square error to ensure good fit in all parts of the curve. The optimized modeling parameters were found by minimizing the mean square error and is given in Table 4. The equivalent stress-equivalent plastic strain curve up to necking is plotted together with the optimized Voce curve in Figure 17.

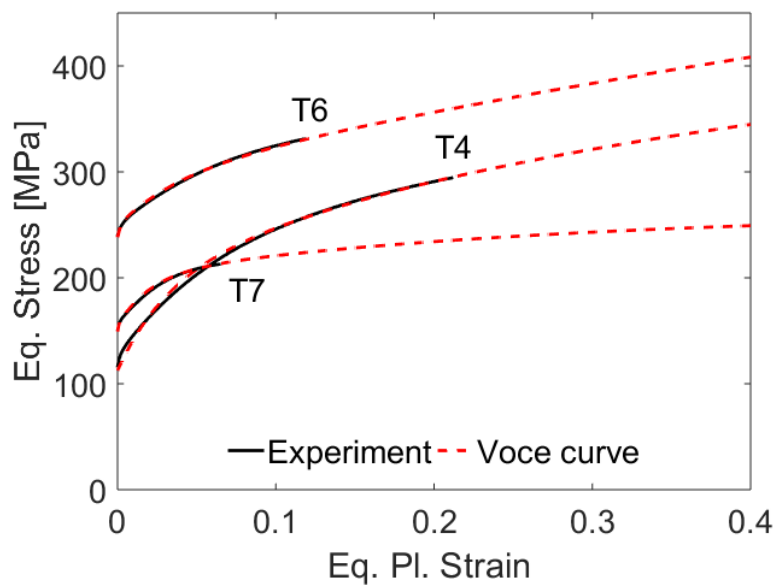


Figure 17: Equivalent stress versus equivalent plastic strain of experiment up to necking along with the calibrated Voce curve.

The CL failure criterion described in the previous section was calibrated based on numerical simulations of the tensile test. The FE model was identical to the one used in calibration of the hardening parameters except for the mesh, which was changed to dimensions  $0.5 \text{ mm} \times 0.5 \text{ mm} \times 0.5 \text{ mm}$ , coinciding with the mesh size used in the blast simulations. The equivalent plastic strain,  $p$ , were extracted from the element exposed to the largest plastic strain in the simulation. This element was the through-thickness centre of the specimen, which was also the element who exhibited the largest value of  $W$ . The failure strain,  $p_f$ , was determined based on the force-displacement curve where the point of failure was set to match the anticipated point from the experimental curve, visualized in Figure 1b. The failure parameter,  $W_c$ , was found by integrating the major principal stress over the equivalent plastic strain to failure and is presented in Table 4 for the three tempers. The slight deviation in elongation at failure among the tensile tests indicates that if calibrated against another tensile test,  $W_c$  would vary and to some extent affect the numerical results.

Table 4: Model parameters for the AA6016 plates in the three tempers.

|         | $\sigma_0$ (MPa) | $Q_1$ (MPa) | $C_1$   | $Q_2$ (MPa) | $C_2$ | $Q_3$ (MPa) | $C_3$ | $W_c$ (MPa) |
|---------|------------------|-------------|---------|-------------|-------|-------------|-------|-------------|
| 6016-T4 | 112.46           | 78.64       | 32.80   | 109.80      | 4.94  | 325.69      | 0.50  | 181.82      |
| 6016-T6 | 238.25           | 11.18       | 539.62  | 46.32       | 24.71 | 398.37      | 0.83  | 155.05      |
| 6016-T7 | 149.20           | 5.89        | 1989.17 | 47.32       | 48.47 | 60.36       | 3.73  | 186.08      |

The strain rate sensitivity of AA6016 has not been examined in this study, however, the rate sensitivity of 6xxx aluminium alloys have been extensively studied in the literature. The degree of strain rate sensitivity was reported to increase for decreasing material strength or for increasing purity [15]. Chen et al. [16] studied the strain rate sensitivity for extruded AA6082 and AA6060 in T6 temper at strain rates up to  $1000 \text{ s}^{-1}$ . Calibration of the strain rate parameter,  $c$ , resulted in a value of 0.0015 and 0.0038 for the two alloys, respectively. Vilamosa et al. [17] studied three 6xxx alloys at various strain rates and temperatures. It was reported a low strain rate sensitivity for the tested alloys at room temperature, substantiating the findings in [16]. Based on these findings, the strain rate parameter was set to  $c = 0.001$  for all simulations in this study. The reference strain rate was set to  $\dot{p}_0 = 5 \times 10^{-4} \text{ s}^{-1}$ , coinciding with the initial strain rate in the tensile test. The parameter controlling the thermal softening was set to  $m = 1$ , indicating a linear degradation of strength for increasing temperature. The effect of including adiabatic heating was investigated by also running isotherm simulations. All material parameters used in the simulations are presented in Table 5, where the rest of the parameters are from the literature as standard values for aluminium.

Table 5: Material constants for AA6016 taken from the literature.

| $E$ (GPa) | $\nu$ | $\rho$ (kg/m <sup>3</sup> ) | $\dot{p}_0$ (s <sup>-1</sup> ) | $c$   | $T_r$ (K) | $T_m$ (K) | $m$ | $c_p$ J/(kg K) | $\chi$ |
|-----------|-------|-----------------------------|--------------------------------|-------|-----------|-----------|-----|----------------|--------|
| 70        | 0.3   | 2700                        | $5 \times 10^{-4}$             | 0.001 | 293       | 923       | 1.0 | 910            | 0.9    |

### 5.3 Finite element modelling

The finite element simulations for the plates subjected to blast loading was conducted using Abaqus/Explicit. A user-defined subroutine (VUMAT) was employed to include the MJC constitutive relation and the CL failure criterion. To save computational time and keep the complexity of the model reasonable, only the blast subjected area of the plate was modelled. The outer boundary of the plate was fixed against displacements to mimic the effect of the clamping plates. The simulations were run with 8-node brick elements with reduced integration with both a random generated sweep mesh and a structural mesh with characteristic element length of 0.5 mm. This resulted in three elements over the thickness and symmetry along the horizontal and vertical axis were utilized when available. The quarter model contained of around 270 000 elements while the full model contained around 1 000 000 elements. The slits were modelled star-shaped where each of end points of the slits where modelled with a single node. The width of the slit then increased towards the centre to 0.1 mm. This modelling option has the advantage of making the meshing of the plate more feasible as well as avoiding bad aspect ratios and distortions of the elements in the vicinity of the slits. Contact was omitted in the model as only the blast exposed area was modelled and contact in the tests took place outside the time of interest in this study. The blast load was applied as a tabulated pressure force where the pressure-time histories were taken from massive plate test where pressure sensors were mounted directly on the plate. The pressure-time histories were curve fitted to the modified Friedlander equation, given as

$$P_r(t) = P_{r,max} \left(1 - \frac{t-t_a}{t_{d+}}\right) \exp\left(\frac{-b(t-t_a)}{t_{d+}}\right) \quad (5)$$

where  $P_{r,max}$  is the peak reflected overpressure,  $t_a$  is the time of arrival of the blast wave at the plate,  $t_{d+}$  is the duration of the positive phase and  $b$  is the exponential decay coefficient. The curve-fitted parameters of the Friedlander equation is taken from an earlier study in the same facility Aune et al. [12] and is given in Table 6.

Table 6: Parameters of the Friedlander equation curve-fitted to the pressure measurements from massive plate tests.

| Test  | $P_{r,max}$ [kPa] | $t_{d+}$ [ms] | $b$   |
|-------|-------------------|---------------|-------|
| M-1.0 | 446.2             | 35.4          | 1.571 |
| M-1.5 | 606.6             | 44.1          | 2.025 |



Failure was introduced by element erosion where the element was removed from the mesh when the damage variable,  $D$ , reached unity in the integration point.

## 6 Results and discussion

### 6.1 Parameter study

An initial mesh sensitivity study was conducted to ensure that the discretization of the plate was sufficient. The number of elements over the thickness was varied from three to six, where the characteristic element length was kept similar to the thickness of the element. Three elements over the thickness proved to give sufficient accuracy at an acceptable computational cost, and was used in the rest of the study. However, analyses with a refined mesh was ran in the cases where the initial model struggled to replicate experiment, to investigate if this solved the discrepancies. Additionally, the design of the mesh was investigated, where both a structured and a random mesh was studied. The differences between the two meshes with a characteristic element size of 0.5 mm is depicted in Figure 18.

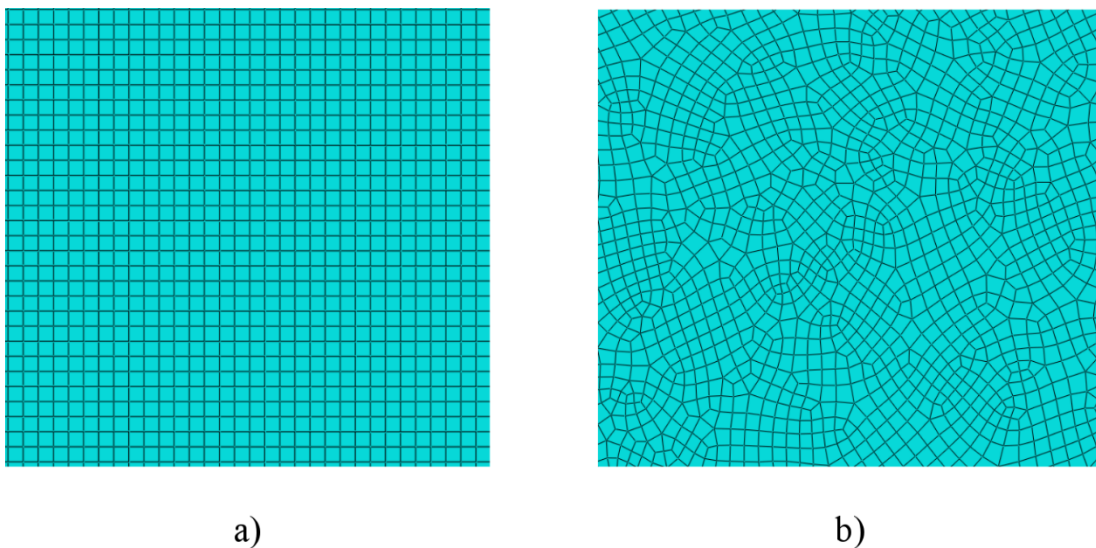


Figure 18: A segment of a) a structured mesh and b) a random mesh used in the numerical simulations.

Since element erosion is used to describe failure in the plate, the design of the mesh plays a significant role in determining the crack path. In the simulations with the structured mesh, it was evident that the propagating cracks were aligned with the orientation of the mesh. This proved to be especially important when the slits were oriented differently from the mesh orientation, resulting in a higher resistance against crack propagation than when the orientations aligned. Overall, it was seen that the

desired crack path could to some extent be provoked by altering the mesh accordingly. It should be noted that a possible approach to minimize this effect is to refine the mesh sufficiently. However, this is not feasible in this situation as the computational cost is far too expensive. Thus, in an attempt to avoid the mesh design effect and to ensure trustworthy results, a random generated mesh were used in this study. Figure 19 shows how the two mesh designs in Figure 18 affect the damage evolution of the plate when plotted on the undeformed geometry. The red colour indicates a failed element.

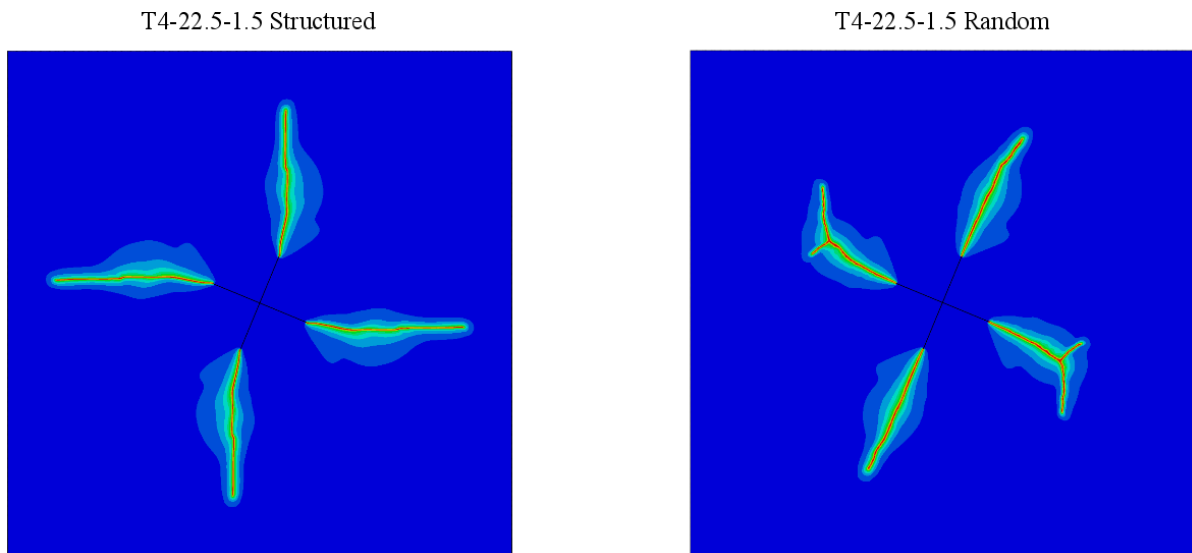


Figure 19: Damage evolution of a T4-22.5-1.5 simulation using both a structured and random mesh design.

## 6.2 Blast simulation results

The focus in the numerical part of the study is to examine the differences in the results between the simulations and experiments. Especially the discrepancies in the structural response and failure mode of the plate is investigated. Apart from the suggestions made in the parameter study in the former section, no further effort is put into enhancing the numerical models in an attempt to improve the agreement to the experimental results. Image series from selected points in time comparing the tests and the simulations in the T4 temper is shown in Figure 20 and Figure 21 for 1.0 MPa and 1.5 MPa firing pressure, respectively. By inspection of the figures, it is evident that the rather simple numerical model is able to replicate most of the tests with satisfying accuracy. However, if studied in detail, discrepancies are seen in some of the models. The simulation deviating the most from the test is the T4-45-1.5, where the wrong failure mode is predicted. The mesh dependence was investigated by running a simulation where the mesh was refined to six elements over the thickness, resulting in a characteristic element length of 0.25 mm and just below 2.7 million elements. However, the same failure mode was predicted as the one with three elements over the thickness and only marginal differences was observed between the two simulations. For the simulations with the highest firing pressure, the effect of the

pressure load acting perpendicular to the load surface is of the most pronounced sources of error, which accumulate error as the surface deforms. This is especially evident in the last frames of the simulations, where the flaps have folded considerably more than in the test. If a flap is deformed sufficiently, one may end up in a situation where the load is acting in the opposite direction of the initial blast load direction, which is obviously wrong. To be able to replicate the final deformed shape of the plates, this effect should be avoided for instance by conducting coupled simulations or manipulate the pressure load to only account for the component in the initial blast load direction.

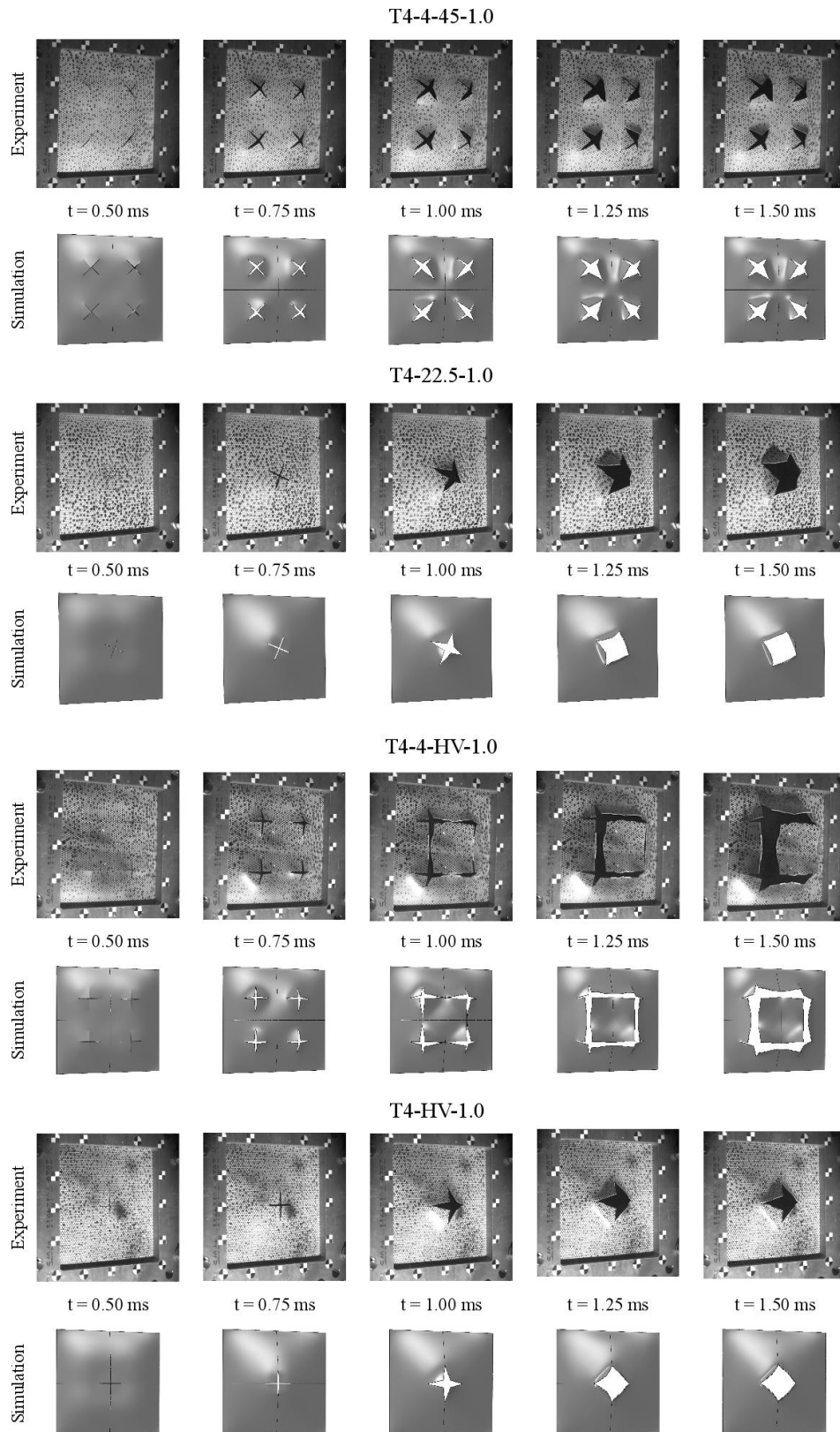


Figure 20: Image series from experiment and simulation of all T4 temper 1.0 MPa firing pressure tests.

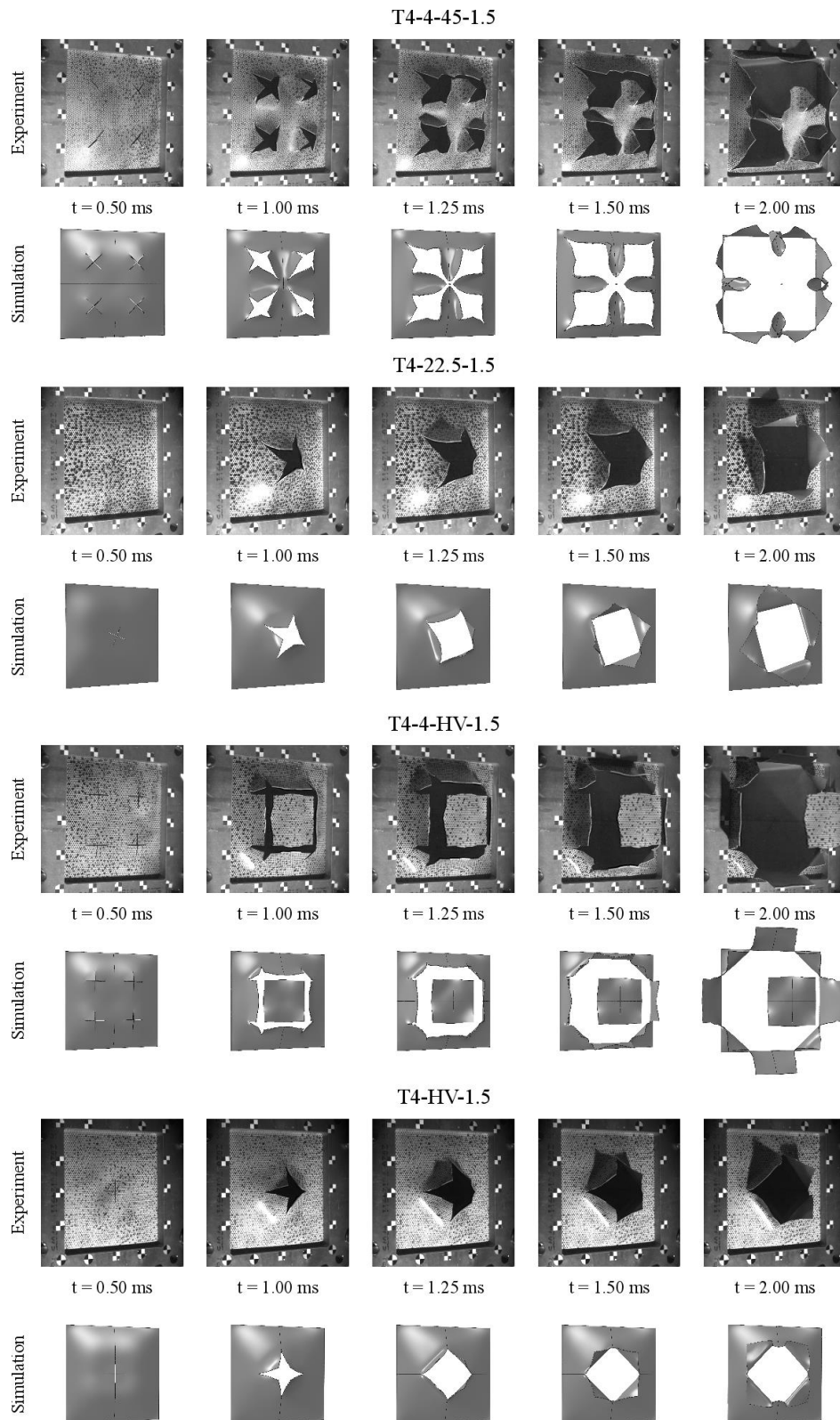


Figure 21: Image series from experiment and simulation of all T4 temper 1.5 MPa firing pressure tests.

Image series from the T6 and T7 temper tests are compared to the numerical results in Figure 22 and Figure 23 for 1.0 and 1.5 MPa firing pressure, respectively. The simulation of the T6-4-45-1.0 test is not able to predict the failure that occurred in the test, and only minor crack propagation was seen in

the numerical results. The cracks in the simulation propagated in the directions of the diagonals, similar to what was observed in the simulation of the T4-4-45-1.0 test. The cracks were initiated at the same point in time in the simulations as in the test, but already at  $t = 1.00$  ms the discrepancies are clear, where two propagating cracks have fused in the experiment already. The numerical results of the T6-22.5-1.0 test on the other hand is in good accordance with the test, where the flaps are folded at the correct point in time. As reported in the experimental results, the failure pattern in the T4-4-45-1.5 and T6-4-45-1.5 tests were similar, and once again the simulation of the latter test predicted a different failure mode than what was observed the test. In the simulation, the cracks propagated along the diagonals of the plate and was folded around each side of the plate. In the test, there is indication of crack propagation along the diagonals towards the centre of the plate, however, the growth of these cracks are halted as cracks propagate between the slits, resulting in the centre of the plate being torn out in the shape of a cross. When the simulation of the T6-4-45-1.5 test is compared to the simulation of the T4-4-45-1.5, the difference in the velocity of the growing cracks is evident. In the latter simulation, the plate is seemingly more resistant to crack propagation when compared to the former. In the simulation of the T6-22.5-1.5 test the response is well predicted up to  $t = 1.0$  ms, but then the propagation of the cracks stop while the flaps continue to fold and a peeling type of failure is seen at  $t = 2.0$  ms.

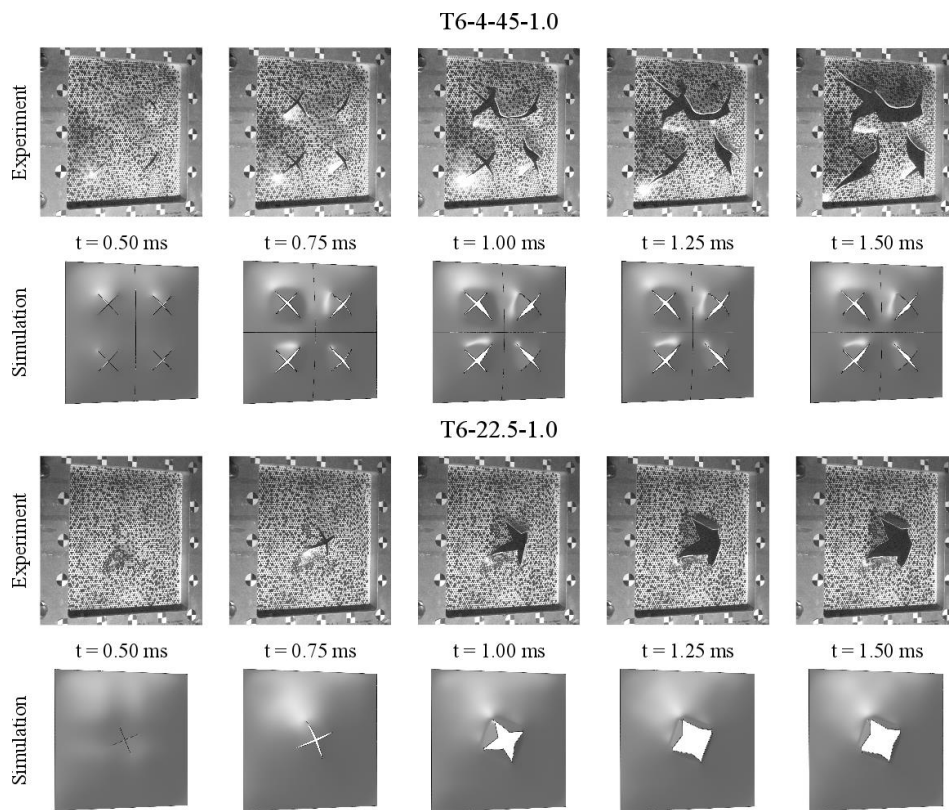


Figure 22: Image series from experiment and simulation of all T6 temper 1.0 MPa firing pressure tests.

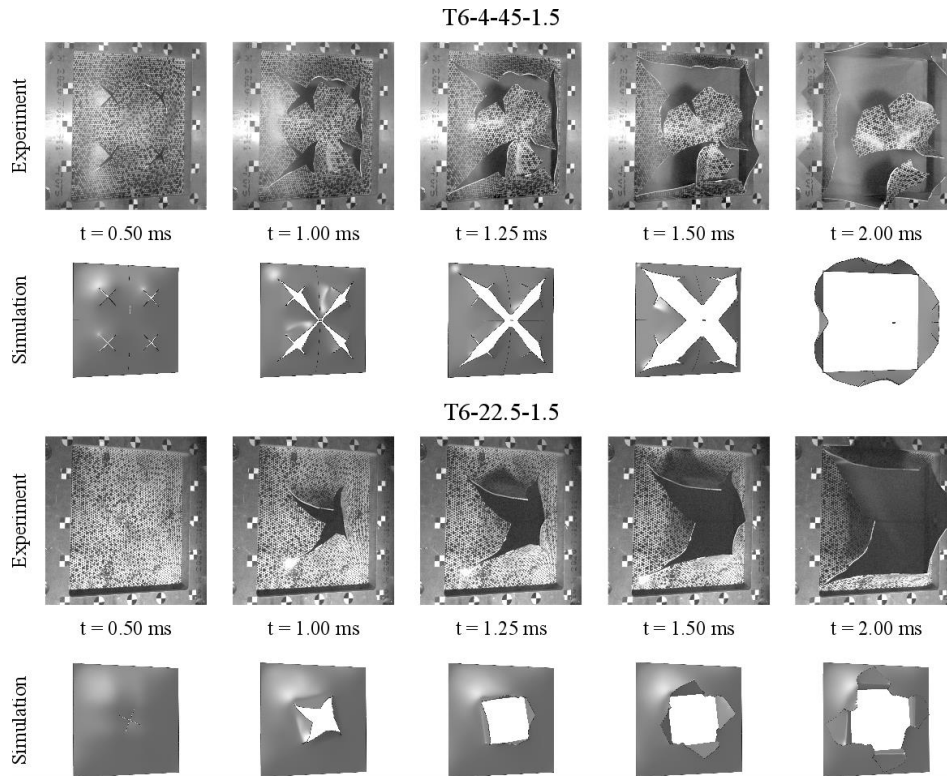


Figure 23: Image series from experiment and simulation of all T6 temper 1.5 MPa firing pressure tests.

Interestingly, absence of complete failure was incorrectly predicted by the simulation of the T6-4-45-1.0 test, while failure was incorrectly predicted by the simulation of the T7-4-45-1.0 test shown in Figure 24. Failure was predicted in the simulation of the T7-4-45-1.5 test in Figure 25, but the same incorrect failure mode as the one seen in the simulation of the T6-4-45-1.5 test was found. In general, the numerical model struggled with predicting the correct failure mode for all tests with this geometry. This suggests that the numerical model is not able to capture the physics in the tests. On the other hand, the numerical simulations are in good agreement with both the T7-22.5 tests, where the structural response is excellent at all points in time. Especially the correspondence between the T7-22.5-1.5 test and simulation was excellent, where the correct curved crack path was accurately predicted in the simulation. The plate is more folded towards the end in the simulations compared to the test, which is expected due to the perpendicular acting pressure load throughout the simulation.

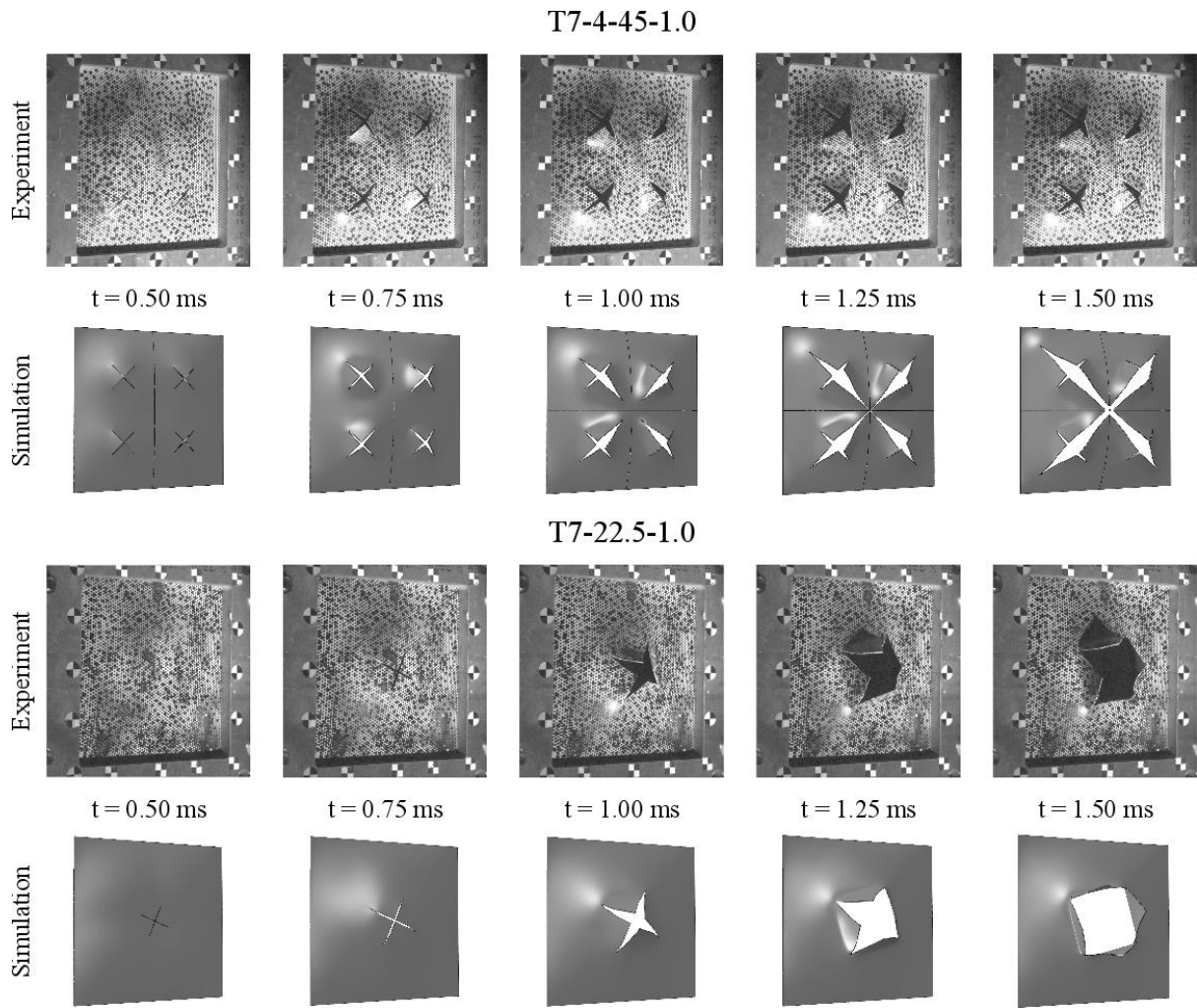


Figure 24: Image series from experiment and simulation of all T7 temper 1.0 MPa firing pressure tests.



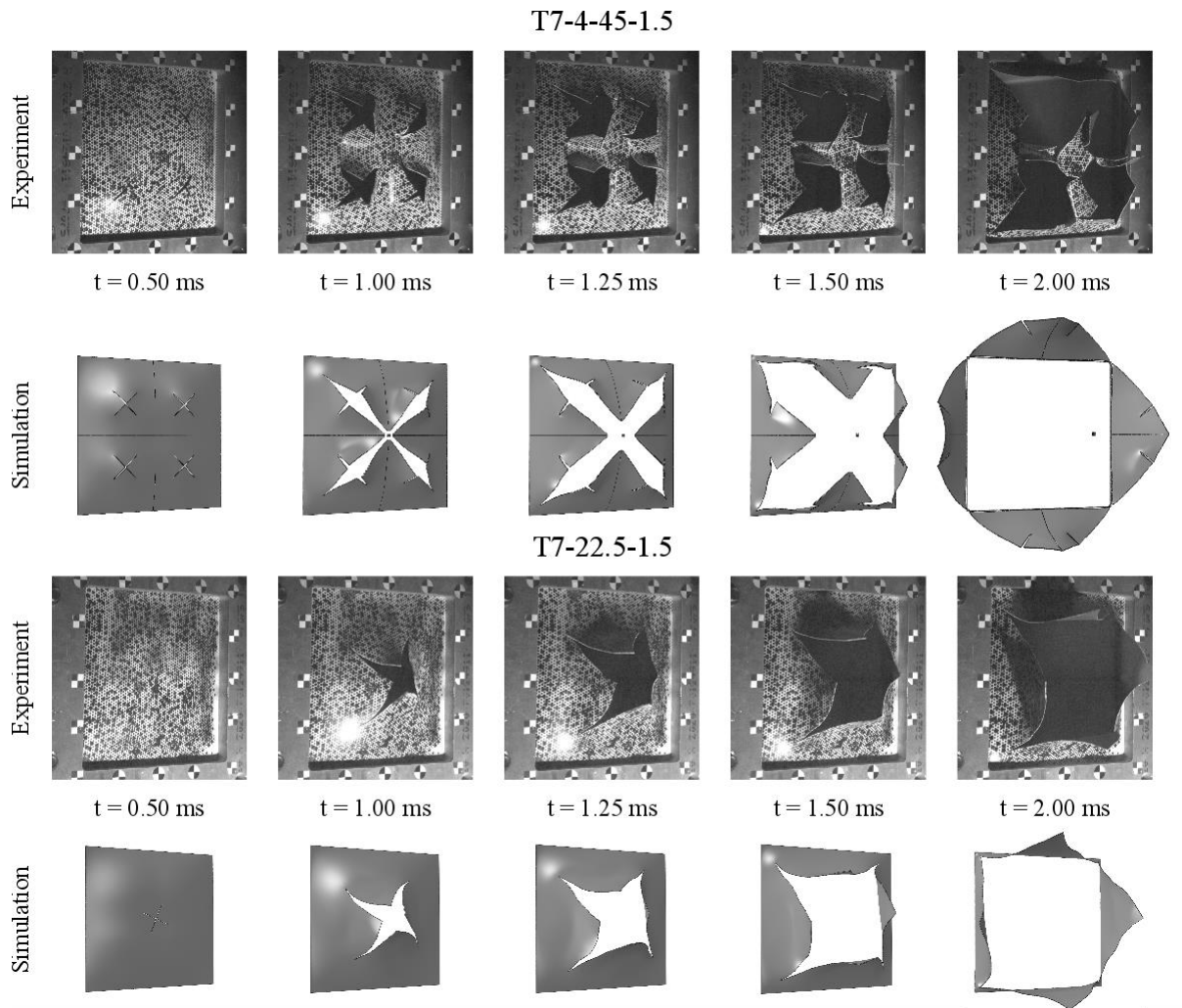


Figure 25: Image series from experiment and simulation of all T7 temper 1.5 MPa firing pressure tests.

The displacement contour plot from the available tests and simulations in the T4 temper is shown in Figure 26. The plates with one slit show a more global response in the simulations than in the experiments. One should have in mind that the end frame of the simulation is two milliseconds after the shock wave impact the plate, and the plate is vibrating at this point due to elastic vibrations. The elastic vibrations are relatively small, but they presumably have an impact on the contour plot. The effect is anticipated to be greater for higher firing pressures. The agreement between the T4-4-45-1.0 simulation and test is good where the trends seen in the experiment were accurately predicted in the simulation. Comparison of the T4-HV-1.5 test and simulation is not shown due to the effect of the perpendicular acting pressure load resulting in self-contact in the plate, making the contour plot useless.

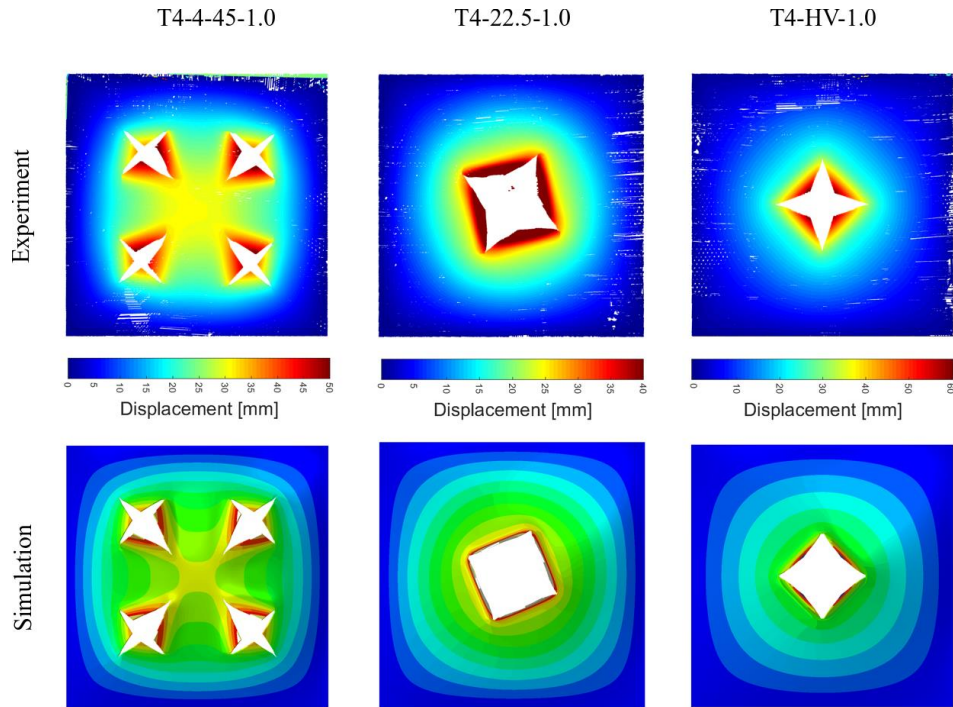


Figure 26: Displacement contour plots from available tests and simulations in T4 temper.

The displacement contour plot from the T6-22.5-1.0 and T7-22.5-1.0 test and simulation is shown in Figure 27. The results from the T6-4-45 and T7-4-45 tests are omitted since either the test or the corresponding simulation experienced complete failure. Similar to the T4 results in Figure 26, both the T6 and T7 simulations predict a more global response compared to the experiments. The discrepancies in the T7-22.5-1.0 are due to the perpendicular pressure load discussed earlier, which affects the deformed state of the plate. Overall, the agreement between the simulations and tests is deemed good, taking into consideration the effects mentioned earlier in this section.

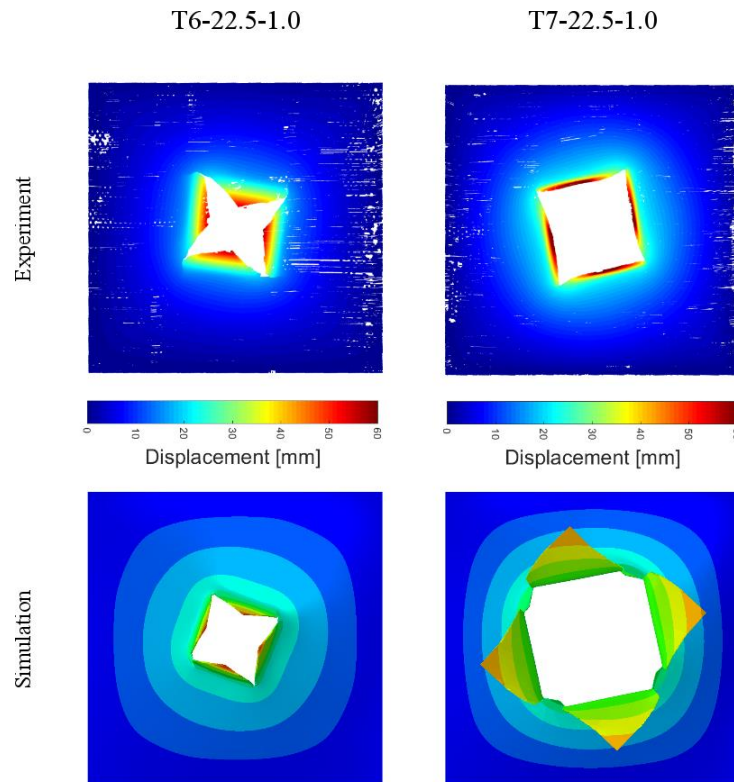


Figure 27: Displacement contour plots from the T6-22.5-1.0 and T7-22.5-1.0 tests and simulations.

To investigate if the progress of the deformation of the plate is accurately predicted by the simulation, a cross-section along the horizontal axis in the middle of the plate is extracted from a T4-4-45-1.0 simulation and test at five different points in time, shown in Figure 28. The response of the plate is accurately predicted to initiate at the boundary of the plate and the correct displacement as seen for  $t = 0.41$  ms. The agreement between the experiment and simulation is excellent all the way to  $t = 1.04$ , which is the maximum displacement in the test. Both the test and the simulation showed minor propagation of cracks, presumed to have negligible influence on the response of the plate. It is evident that the numerical model is able to describe the plasticity in this problem. Unfortunately, this comparison is unavailable for the T6 and T7 tempers, as failure occurred in either the test or the corresponding simulation.

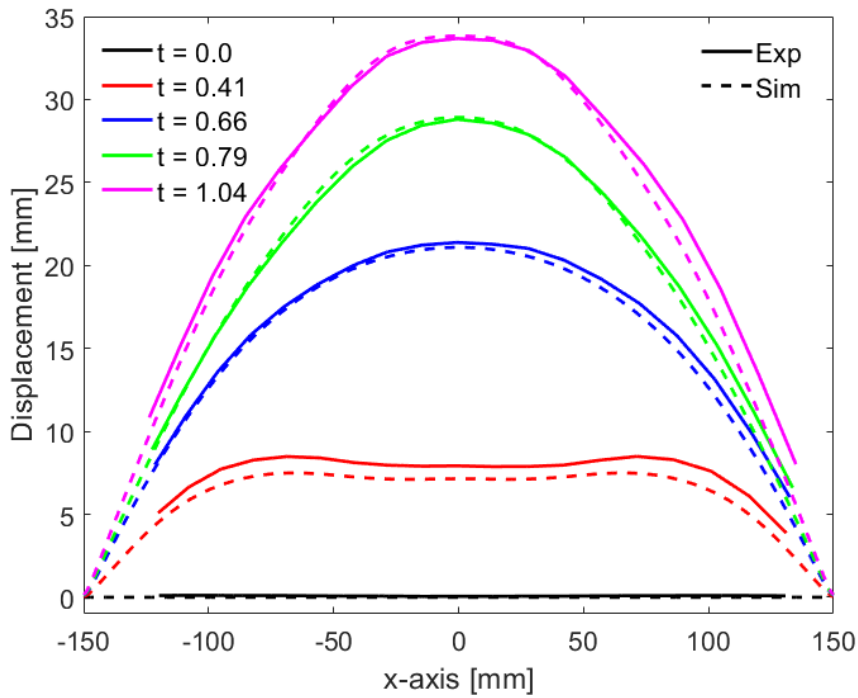


Figure 28: This is the caption

To investigate the failure mode predicted in the T4-4-45-1.5 simulation, contour plots of the triaxiality, Lode and equivalent plastic strain is plotted for the upper right quarter of the plate in Figure 29. The plots are taken from  $t = 0.5$  ms to  $0.8$  ms and shows the evolution of the first cracks. By inspection of the figure, one can see that the cracks are propagating in elements with a triaxiality between  $0.5$  to  $0.67$  and a Lode around  $0$ , suggesting that the stress state is approximately plane stress for these elements. The equivalent plastic strain is accumulating in front of all slits and cracks are seen to propagate from all of them. However, between  $t = 0.7$  to  $t = 0.8$  ms the crack propagation becomes critical along the diagonals of the plate, while it stagnates for the two other slits. The stress state in front of the four slits is comparable, even though the cracks only propagate along the two aligned with the diagonal. To predict the same failure mode as seen in the experiment of this plate, the cracks would have had to propagate at the two opposite slits. By inspection of the figure, one can see that the cracks from these slit are deflecting along the horizontal and vertical axis of the plate as observed in the test, before they stagnate. The marginal difference in the stress state between the two propagating cracks and the two stagnating cracks suggest that a more accurate failure criterion may be able to predict the correct failure mode for this geometry.

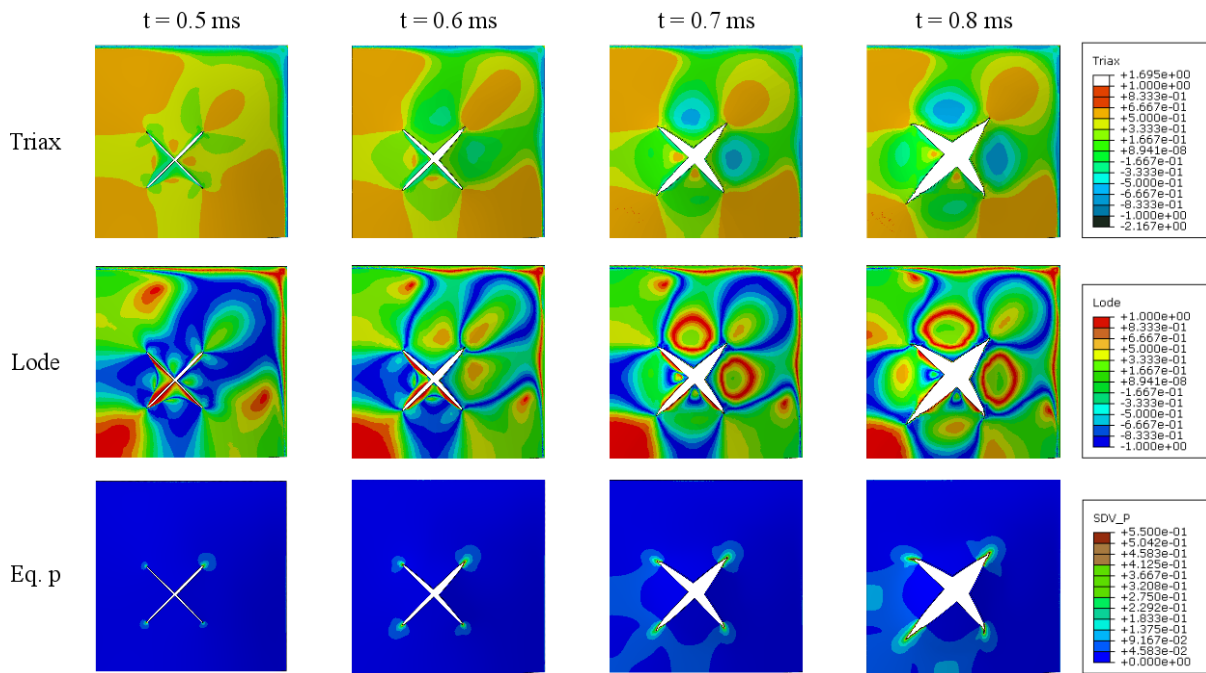


Figure 29: Contour plots of the triaxiality, Lode and equivalent plastic strain for a quarter T4-4-45-1.5 simulation at selected points in time.

## 7 Conclusion

This study have presented an experimental programme including material tests and blast tests of 1.5 mm thick AA6016 plates in three different tempers. The tests on the blast-loaded plates were divided in two parts, both conducted in the SIMLab shock tube facility. Part one of the study consisted of eight tests on T4 plates with four different pre-cut slit geometries at two different firing pressures. Part two consisted of eight tests on T6 and T7 plates with two of the pre-cut slit geometries from part one and similar firing pressures. High-speed cameras captured the blast events, and together with synchronized pressure sensors along the tube used to study the structural response of the plate and the incoming and reflected shock wave, respectively. 3D-DIC was employed to extract deformations from the plate and selected plates were 3D-scanned to arrange visualisation of the plates. A total of 27 tensile tests were conducted with triplicate tests in the  $0^\circ$ ,  $45^\circ$  and  $90^\circ$  with respect to the rolling direction for each temper. The tensile tests exhibited a nearly isotropic material behaviour among the three tempers yet, the elongation at failure within the tempers displayed a small variation. The effect of the different pre-cut slit geometries was evident, where either rotating the slit(s) or increasing the amount of slits displayed prominent differences on the structural response. The most distinct effect is seen for the plates with four slits at the lowest firing pressure, where the plate with slits oriented along the horizontal and vertical axis experienced complete failure opposed to the plate with the slits oriented  $45^\circ$ , which only experienced minor propagation of cracks. The effect of temper was prominent for the two pre-cut slit

geometries tested. Material strength was seen to be of less importance to resist propagation of cracks, where in one test case, the plate with the highest strength was the only one to experience complete failure. This temper also exhibited the lowest ductility, which seemingly is an important material property with respect to resisting failure. Cracks initiated at similar points in time independent of material properties, however high strength and low ductility apparently increases the velocity of the propagating cracks compared to a plate with contrary material properties. Based on the limited amount of tests and the lack of repetitions, the current study is not comprehensive enough to draw any conclusion, however, all the conducted tests supports the findings made.

Numerical simulations were conducted using a modified Johnson-Cook plasticity model and the uncoupled failure criterion proposed by Cockcroft and Latham. Element erosion was used as failure method and the load was applied as a pressure on the plate surface. A refined volume element mesh with a characteristic length of 0.5 mm was generated using a sweep technique. The numerical simulation were able to predict the correct failure modes for all geometries except one, and the overall agreement with the tests was good. Cross-section plots from the test and simulation revealed that the progress of the deformation was accurately predicted in the numerical model, substantiating that the constitutive model was able to describe the plasticity in the test. In general, the numerical model gives a good indication of the amount of failure in a test, even though the correct failure mode is not always predicted.

## Acknowledgment

The authors gratefully appreciate the financial support from NTNU and the Research Council of Norway through the FRINATEK Programme, Project No. 250553 (FractAI). The authors would also like to thank Mr. Trond Auestad for assistance with accomplishing the experimental programme.

## References

- [1] Rakvåg K.G, Underwood N.J, Schleyer G.K, Børvik T, Hopperstad O.S. Transient pressure loading of clamped metallic plates with pre-formed holes. *International Journal of Impact Engineering* 2013; 53: 44-55
- [2] Li Y, Weiguang W, Haiqing Z, Zhen W, Zhipeng D. The influence of different pre-formed holes on the dynamic response of square plates under air-blast loading. *Engineering Failure Analysis* 2017; 78: 122-133
- [3] Aune V, Valsamos G, Casadei F, Langseth M, Børvik T. On the dynamic response of blast-loaded steel plates with and without pre-formed holes. *International Journal of Impact Engineering* 2017; 108: 27-46
- [4] Zhang C, Cheng Y, Zhang P, Duan X, Liu J, Li Y. Numerical investigation of the response of I-core sandwich panels subjected to combined blast and fragment loading. *Engineering Structures* 2017; 151: 459-471
- [5] Langdon G. S, Lee W. C, Louca L. A. The influence of material type on the response of plates to air-blast loading. *International Journal of Impact Engineering* 2015; 78: 150-160

- [6] Holmen J. K, Johnsen J, Hopperstad O. S, Børvik T. Influence of fragmentation on the capacity of aluminum alloy plates subjected to ballistic impact. *European Journal of Mechanics A/Solids* 2016; 55: 221-233
- [7] Forrestal M. J, Børvik T, Warren T. L. Perforation of 7075-T651 aluminum armor plates with 7.62 mm APM2 bullets. *Experimental mechanics* 2010; 50: 1245-1251
- [8] Holmen J. K, Johnsen J, Jupp S, Hopperstad O. S, Børvik T. Effects of heat treatment on the ballistic properties of AA6070 aluminium alloy. *International Journal of Impact Engineering* 2013; 57: 119-133
- [9] Granum H, Myhr O. R, Børvik T, Hopperstad O. S. Nanostructure-based finite element analyses of aluminium profiles subjected to quasi-static axial crushing. *Thin-Walled Structures* 2018; 131: 769-781
- [10] Gruben G, Hopperstad O. S, Børvik T. Simulation of ductile crack propagation in dual-phase steel. *International Journal of Fracture* 2013; 180: 1-22
- [11] Fagerholt E. Field measurements in mechanical testing using close-range photogrammetry and digital image analysis. PhD thesis, Norwegian University of Science and Technology, 2012
- [12] Aune V, Fagerholt E, Langseth M, Børvik T. A shock tube facility to generate blast loading on structures. *International Journal of Protective Structures* 2016; 7(3): 340-366
- [13] Børvik T, Hopperstad O.S, Berstad T, Langseth M. A constitutive model of viscoplasticity and ductile damage for impact and penetration. *European Journal of Mechanics A/Solids* 2001; 20: 685-712
- [14] Cockcroft M. G, Latham D. J. Ductility and workability of metals. *Journal of the Institute of Metals*, 1968; 96: 33-39
- [15] Zukas J. A, Nicholas T, Swift H. F. *Impact Dynamics*. Krieger Publishing Company, 1992.
- [16] Chen Y, Pedersen K. O, Clausen A. H, Hopperstad O. S. An experimental study on the dynamic fracture of extruded AA6xxx and AA7xxx aluminium alloys. *Materials Science and Engineering A* 2009; 523: 243-262
- [17] Vilamosa V, Clausen A. H, Børvik T, Skjervold S. R, Hopperstad O. S. Behaviour of Al-Mg-Si alloys at a wide range of temperatures and strain rates. *International Journal of Impact Engineering* 2015; 86: 223-239